Astronomy & Astrophysics

Evidence of apsidal motion and a possible co-moving companion star detected in the WASP-19 system

L. M. Bernabò[1] , Sz. Csizmadia[1,2] , A. M. S. Smith[1] , H. Rauer[1,3,4] , A. Hatzes[5] , M. Esposito[5] ,
D. Gandolfi[6] , and J. Cabrera[1]

[1] Institute of Planetary Research, German Aerospace Center (DLR), Rutherfordstrasse 2, 12489 Berlin, Germany
e-mail: lia.bernabo@dlr.de
[2] ELKH-SZTE Stellar Astrophysics Research Group, 6500 Baja, Szegedi út Kt. 766, Hungary
[3] Zentrum für Astronomie und Astrophysik, Technische Universität Berlin, Hardenbergstr. 36, 10623 Berlin, Germany
[4] Institut für Geologische Wissenschaften, Freie Universität Berlin, 12249 Berlin, Germany
[5] Thüringer Landessternwarte Tautenburg, Sternwarte 5, 07778 Tautenburg, Germany
[6] Dipartimento di Fisica, Università degli Studi di Torino, Via Pietro Giuria, 1, 10125 Torino, Italy

ABSTRACT

Context. Love numbers measure the reaction of a celestial body to perturbing forces, such as the centrifugal force caused by rotation, or tidal forces resulting from the interaction with a companion body. These parameters are related to the interior density profile. The non-point mass nature of the host star and a planet orbiting around each other contributes to the periastron precession. The rate of this precession is characterized mainly by the second-order Love number, which offers an opportunity to determine its value. When it is known, the planetary interior structure can be studied with one additional constraint beyond the mass, radius, and orbital parameters.

Aims. We aim to re-determine the orbital period, eccentricity, and argument of the periastron for WASP-19Ab, along with a study of its periastron precession rate. We calculated the planetary Love number from the observed periastron precession rate, based on the assumption of the stellar Love number from stellar evolutionary models.

Methods. We collected all available radial velocity (RV) data, along with the transit and occultation times from the previous investigations of the system. We supplemented the data set with 19 new RV data points of the host star WASP-19A obtained by HARPS. Here, we summarize the technique for modeling the RV observations and the photometric transit timing variations (TTVs) to determine the rate of periastron precession in this system for the first time.

Results. We excluded the presence of a second possible planet up to a period of $\sim$4200 d and with a radial velocity amplitude bigger than $\simeq$1 m s^{-1}. We show that a constant period is not able to reproduce the observed radial velocities. We also investigated and excluded the possibility of tidal decay and long-term acceleration in the system. However, the inclusion of a small periastron precession term did indeed improve the quality of the fit. We measured the periastron precession rate to be 233^{+25}_{-35} ″d^{-1}. By assuming synchronous rotation for the planet, it indicates a k_2 Love number of $0.20^{+0.02}_{-0.03}$ for WASP-19Ab.

Conclusions. The derived $k_{2,p}$ value of the planet has the same order of magnitude as the estimated fluid Love number of other Jupiter-sized exoplanets (WASP-18Ab, WASP-103b, and WASP-121b). A low value of $k_{2,p}$ indicates a higher concentration of mass toward the planetary nucleus.

Key words. planets and satellites: dynamical evolution and stability – planets and satellites: interiors – planet-star interactions

1. Introduction

The understanding of planetary interiors constitutes one of the four major challenges of contemporary exoplanetary science (Schneider 2018). It is crucial for assessing their potential habitability, formation, and evolution. Interior processes play an essential role in creating and maintaining the physical conditions that are required to support life (see, e.g., Van Hoolst et al. 2019). They are useful for determining which planetary formation process is most plausible; namely, whether it is core accretion (Pollack et al. 1996 and references therein) or gravitational instability (Boss 1997 and references therein). According to the former, the accretion of planetesimals would result in the formation of a core comprised of heavy elements. On the other hand, planets forming through disc instability can rapidly accrete gas. These two scenarios lead to different core sizes. The size of the core is related to the second order fluid $k_{2,p}$ Love number (Love 1911), as explained in Becker & Batygin (2013). Knowledge of the interior of a giant planet can help us distinguish between these two scenarios, in addition to its Love number, as we describe in this work.

Love numbers can also be used to break the known mass-radius-composition degeneracy of exoplanets (Baumeister et al. 2020). When an exoplanet is characterizable both by transit and radial velocity techniques, we can derive its radius and mass – and, thus, the planetary mean density. However, mass, radius and mean density are degenerate when it comes to determining the interior structure of bodies, such as the radial density, temperature, pressure, and composition profiles. We can find multiple solutions for the planetary interior producing the same planetary total mass and radius (see, e.g., Valencia et al. 2007; Wagner et al. 2011; Damasso et al. 2018). This kind of degeneracy can be decreased based on the strong assumption that the planet and its host star share the same metallicity (Dorn et al. 2015).

For Solar System planets, the degeneracy between mean density and interior structure can be reduced by in situ measurements of the gravitational field, as well as by seismic measurements, such as InSight (Banerdt et al. 2020), and by

observations of moon motions. However, for exoplanets, gravitational moments cannot be measured. Hence, Love numbers were proposed as further observables in exoplanetary interior studies (see, e.g., Batygin et al. 2009; Ragozzine & Wolf 2009 and references therein), as has already been applied to eclipsing binary stars systems (see Russell 1928 and references therein). These authors measured the deformations and mass re-distribution inside the planet due to the tidal interaction with the host star. As shown by Baumeister et al. (2020), thanks to the knowledge of the second-order fluid Love number of the planet, we can better infer the distribution of possible thickness of each interior layer.

In this work, we employ a technique used by Csizmadia et al. (2019), which we further refined to determine $k_{2,p}$ from periastron precession. This precession is derived from radial velocity (RV) measurements and transit and occultation mid-times. We apply it to the system WASP-19 based on an approach that requires the calculation of the secular evolution of the orbital elements, which is related to the mass distribution of the star and the planet through their second-degree Love numbers.

This paper is organized as follows. Section 2 and Appendix A present the theory of apsidal motion. Section 3 describes the system WASP-19 and provides evidence of a possible companion star in the WASP-19 system. In Sect. 4, we describe archival transit and occultation timing observations as well as the archival radial velocity investigations of the system which are supplemented by our recent RV study of the system. Section 5 contains our data analysis along with the search for a second planetary companion. Our conclusions are given in Sect. 6.

2. Apsidal motion

Apsidal motion, namely, the secular perturbation in the argument of periastron, can be detected either in RV or in TTV datasets (or their combination) to constrain the internal structure of planets. This type of analysis on RVs was introduced by Kopal (1959, 1978). Here, we make use of such equations, however, we have rewritten them in a way that allows them to be directly applied to the observed data sets. We describe their derivations more in detail in Appendix A.

The total rate of apsidal advance is the result of the three contributions:

$$\dot{\omega} = \frac{d\omega}{dt} = \frac{d\omega_{GR}}{dt} + \frac{d\omega_{tidal}}{dt} + \frac{d\omega_{rot}}{dt}. \tag{1}$$

The general relativistic term $d\omega_{GR}/dt$ (Einstein 1915) is:

$$\frac{d\omega_{GR}}{dt} = \frac{6\pi G M_\star}{ac^2(1-e^2)} \frac{1}{P_a}, \tag{2}$$

where G is the gravitational constant, $M_\star$ the mass of the star, a and e the semi-major axis and eccentricity of the orbit, c the speed of light in vacuum, and P_a the anomalistic period.

The secular perturbations of the tidal and rotational components $d\omega_{tidal}/dt$ and $d\omega_{rot}/dt$ are derived in Appendix A and can be expressed more explicitly if approximated to the second order, as in Csizmadia et al. (2019):

$$\frac{d\omega_{tidal}}{dt} \simeq \frac{15}{2} \frac{n}{(1-e^2)^5} \left[\frac{m_p}{M_\star} k_{2,\star} \left(\frac{R_\star}{a} \right)^5 \right.$$
$$\left. + \frac{M_\star}{m_p} k_{2,p} \left(\frac{R_p}{a} \right)^5 \right] \left(1 + \frac{3}{2}e^2 + \frac{1}{8}e^4 \right), \tag{3}$$

Table 1. Expected gravitational, rotational and tidal contribution to the periastron precession in the extreme Love number cases (mass-point and homogeneous planet) and the corresponding apsidal motion period, assuming synchronous rotation for the planet.

	$k_{2,p} = 0.01$	$k_{2,p} = 1.5$
$\dot{\omega}_{GR}$	2.85 ″ d^{-1}	2.85 ″ d^{-1}
$\dot{\omega}_{tid,\star}$	0.47 ″ d^{-1}	0.47 ″ d^{-1}
$\dot{\omega}_{rot,\star}$	0.15 ″ d^{-1}	0.15 ″ d^{-1}
$\dot{\omega}_{tid,p}$	10.53 ″ d^{-1}	1580.16 ″ d^{-1}
$\dot{\omega}_{rot,p}$	0.70 ″ d^{-1}	105.46 ″ d^{-1}
Total $\dot{\omega}$	14.70 ″ d^{-1}	1689.10 ″ d^{-1}
Period	241.25 yr	2.10 yr

and

$$\frac{d\omega_{rot}}{dt} \simeq \frac{1}{2} \frac{n}{(1-e^2)^2} \left[\left(\frac{P_{orb}}{P_{rot,\star}} \right)^2 k_{2,\star} \left(\frac{R_\star}{a} \right)^5 \left(1 + \frac{m_p}{M_\star} \right) \right.$$
$$\left. + \left(\frac{P_{orb}}{P_{rot,p}} \right)^2 k_{2,p} \left(\frac{R_p}{a} \right)^5 \left(1 + \frac{M_\star}{m_p} \right) \right]. \tag{4}$$

In these equations, n is the mean motion, m_p and R_p the mass and radius of the planet, $R_\star$ the radius of the star, and $P_{rot,p}$ and $P_{rot,\star}$ are the rotational periods of the two components. Also, $k_{2,p}$ and $k_{2,\star}$ are their second-order fluid Love number corresponding to the double the apsidal motion constant (Csizmadia et al. 2019):

$$k_{2,i} = 2k_{2,aps,i}, \tag{5}$$

both for the star ($i = \star$) and the planet ($i = p$). These two equations were obtained by Sterne (1939). Just as in Eq. (A.8), it is assumed that the rotational axis of both components are perpendicular to the orbital plane.

Regardless of whether the stellar and planetary rotation is direct or retrograde, the corresponding terms in Eq. (4) are positive, therefore they cause the apsidal line to advance. Assuming the values of the orbital parameters of WASP-19Ab from literature and the Love number of the star from Claret (2004), we calculated the amplitude of the general relativity term and the stellar tidal and rotational contributions, as reported in Table 1. Moreover, a first estimate for the planet can be calculated assuming synchronous rotation for the planet and $k_{2,p}$ between the values 0.01–1.5 (corresponding to the extreme cases of a mass point and a homogeneous body, respectively). The total contribution is between about 14.71–1689 ″d^{-1} $\simeq$ 0.0041–0.479° d^{-1}, respectively when assuming $k_{2,p}$=0.01 and $k_{2,p}$ = 1.5. The apsidal motion period $U = 2\pi/\dot{\omega}$ is therefore between $\simeq$2.10 and $\simeq$41.25 yr.

The equations in Appendix A show that the angle of periastron ω oscillates over one orbital period but also shows a gradual long-term change that can be retrieved in the RV observations. Due to the finite length of the typical datasets of observations (12 yr in the case of WASP-19Ab), in RV datasets, the change in the angle of periastron ω can be retrieved in the radial velocity of the star (see, e.g., Jackson et al. 2008 for more details on the timescales). In long baselines of observations, all orbital elements must be considered along with periastron precession. As described in Kopal (1978), they include the change in semi-major axis (tidal decay), eccentricity (circularization) and time of periastron passage. The semi-major axis and its eccentricity would diminish in value and the time of periastron passage is shifted in time.

Table 2. WASP-19A and its stellar companion

Parameter	WASP-19A	WASP-19B
Gaia DR3 ID	5411736896952029568	5411725145916602496
Apparent separation (″)	0.0	68.0347 ± 0.0009
Gaia G-magnitude	12.1012	20.8859
Gaia BP − RP colour	0.953 ± 0.001	2.213 ± 0.12
pmRA (mas yr^{-1})	−35.4571 ± 0.0089	−35.33 ± 1.18
pmDec (mas yr^{-1})	17.378 ± 0.009	18.22 ± 1.30
Parallax (mas)	3.7516 ± 0.0090	1.92 ± 1.16
Distance (pc)[*]	266.54 ± 0.64	487^{+564}_{-184}
Projected physical separation (AU)	0.0	19976 ± 48
Spectral type[†]	G8V	M2V – M6V

Notes. [*] Assuming no extinction. [†] Assuming that the companion is also a star on the main-sequence.

3. WASP-19Ab

3.1. The system

The planet WASP-19Ab, hosted by the bright, active G-dwarf star (V = 12.3, Zacharias et al. 2012 and $T_{\text{eff},\star} \simeq 5568$ K, Torres et al. 2012), was discovered through the transit method by the Wide Angle Search for Planets (WASP)-South observatory (Hebb et al. 2010). It is a hot Jupiter with mass $m_{\text{p}} = 1.139 \, M_{\jupiter}$, inflated radius $r_{\text{p}} = 1.410 \, R_{\jupiter}$ (Mancini et al. 2013) and orbital period $P_{\text{orb}} \simeq 0.79$ d.

So far, the system is among the best studied from the point of view of orbital and planetary parameters (e.g., Lendl et al. 2013; Mancini et al. 2013; Sedaghati et al. 2015, 2017) and atmosphere characterization (very pronounced water absorption, Huitson et al. 2013; Sedaghati et al. 2017, and titanium oxide detected in the transmission spectrum, Sedaghati et al. 2017). The proximity of WASP-19Ab to its host star results in significant tidal interaction that may govern the evolution of the planetary orbit, which makes the system a good candidate for our study.

Based on transit observations, certain studies have suggested the possibility of variations in the mid-transit time. Mancini et al. (2013) suggested a non-linear ephemeris. However, Petrucci et al. (2020) discarded orbital decay with 74 complete transit light curves spanning over ten years of observations. Moreover, as described more in detail in Sect. 5.1, Cortés-Zuleta et al. (2020) used transit timing variations (TTVs) to infer an upper mass limit for an additional candidate planetary companion in the system.

3.2. Companion star: WASP-19B

We searched the catalogue of the third *Gaia* data release (DR3) (Gaia Collaboration 2016, 2023) for possible co-moving companions to WASP-19A. We searched all objects within 4′ of the target, which corresponds to a physical separation of around 0.3 pc at the distance of WASP-19A, for those with compatible parallax (θ) and proper motions (PM). Only one object was found to have parallax and proper motion values in both the RA (α) and Dec (δ) directions that are compatible with those of the target to within 5σ. This object (*Gaia* DR3 ID = 5411725145916602496), which is 8.8 magnitudes fainter in the *G*-band, has a parallax that differs from that of WASP-19A by 1.6 σ and PM$_\alpha$ and PM$_\delta$ values differing by just 0.1 σ and 0.6 σ respectively. This star is found in the southernmost part of the south-east region of WASP-19A, at a separation of 68″. The magnitude and BP-RP colour of the companion suggests that this star is a mid M-dwarf,

with a best matching spectral type for the magnitude of M6V and for the colour M2V, using the updated table[1] of Pecaut & Mamajek (2013).

To estimate the probability of this putative companion arising from a chance matching of WASP-19 in parallax and proper motions, we searched a much larger area of sky in *Gaia* DR3, still centered on WASP-19, but with a radius of 2°. This produced 77 objects (including the companion; hereafter: 'WASP-19B') that match WASP-19 within 5σ in all of θ, PM$_\alpha$, and PM$_\delta$. This implies that there is an 8.6% chance of finding a matching object within our initial search radius of 4′, and just a 0.7% chance of finding an object as close as WASP-19B. Relaxing the 5σ limit to 3σ changes these probabilities to 2 and 0.16%, respectively. Furthermore, none of these additional matches, all of which are more than ten times further from WASP-19A than WASP-19B, demonstrate as good a match as WASP-19B. Mathematically, this is expressed as WASP-19B having the lowest value of $\sigma_{\text{tot}} = \sigma_\theta + \sigma_{\text{PM}_\alpha} + \sigma_{\text{PM}_\delta}$, where for each parameter, X (where X stands for θ, PM$_\alpha$, PM$_\delta$) $\sigma_X = \frac{|X_1 - X_2|}{\sqrt{\sigma_{X_1}^2 + \sigma_{X_2}^2}}$, where $X_1 \pm \sigma_{X_1}$ and $X_2 \pm \sigma_{X_2}$ are the values and uncertainties of parameter X for WASP-19 and its companion, respectively. We recognise that the uncertainty on the parallax of WASP-19B is relatively large. Even if WASP-19B is likely to be a true, gravitationally bound, companion to WASP-19A, some doubt remains as to whether it truly is a bound companion to WASP-19A. We adopted the planet name WASP-19Ab because it orbits around the brighter primary star. Details of WASP-19B are given in Table 2. With Eq. (9) of Csizmadia et al. (2019), we also determined that the effect of the companion star on the radial velocity of star A is negligible. Star B may be the cause of the presence of an eccentricity different from zero in the orbit on the transiting planet. While tidal interaction leads to circularization, the excitation of the orbit due to a distant companion might prevent it, as discussed in detail in Appendix B.

4. Observations

4.1. Transits and occultations

Mid-transit and occultation times used in this paper are listed in Tables C.1–C.2. We collected publically available data, including some amateur observations listed in the TRansiting ExoplanetS

---

[1] https://www.pas.rochester.edu/~emamajek/EEM_dwarf_UBVIJHK_colors_Teff.txt

Table 3. Radial velocity datasets used in this work.

ID	N_{obs} (out of transit)	Instrument	Reference
1	34 (30)	Coralie	Hebb et al. (2010)
2	3 (2)	Coralie	Hellier et al. (2011)
3	36 (21)	HARPS	Hellier et al. (2011)
4	20 (6)	PFS	Albrecht et al. (2012)
5	3 (3)	HIRES	Knutson et al. (2014)
6, 7	88 (16, 6)	ESPRESSO	Sedaghati et al. (2021)
8	19 (15)	HARPS	This work

Notes. RV datasets are described with ID number, number of points, instrument and reference for the publication of the corresponding data and results. In brackets, one can find the number of out-of-transit as those are the only RV datapoints that are used in the fit.

Fig. 1. Radial velocity observations of WASP-19Ab, time vs. radial velocities, with corresponding observational errorbars. The different data sets (see Sect. 4) are represented by different colours. Between the datasets, there are significant offsets between different instruments and studies. They have been removed accordingly to the results in Table 4.

and CAndidates (TRESCA)[2] project database, part of the Exoplanet Transit Database (Poddaný et al. 2010). In particular, we included amateur data that were selected by Mancini et al. (2013) and other high-quality data showing a clear light curve without gaps. As detailed in the tables, we also re-analyzed some transits with the Transit and Light Curve Modeller (TLCM, Csizmadia 2020).

The time unit of each mid-transit and mid-occultation time was carefully checked and eventually converted into BJD$_{TDB}$ (barycentric Julian date, in the barycentric dynamical time system). The difference between BJD$_{UTC}$ and BJD$_{TDB}$ depends on the number of leap seconds (Eastman et al. 2010). For our dataset, it is around one minute. If the time unit used in the reference paper was not clear, the main author was contacted and the issue was clarified; otherwise, the data were discarded and not reported here. We used the estimated mid-times for each primary transit and occultation to evaluate whether they exhibit deviations from a Keplerian orbit over a long baseline of observations (see Sect. 5.2 for more details) as well as to constrain the sidereal period of the planet.
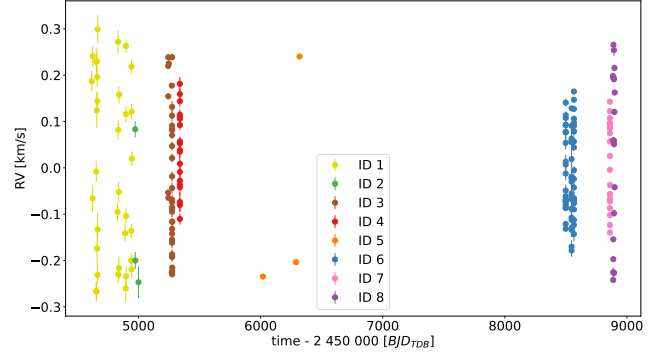
4.2. RVs

We collected all available radial velocity measurements from 2008 onward and we present new RV observations (see ID 8 below). Information on the RV observations are listed in Table 3 and the complete datasets are shown in Appendix D.

Here, we list the main details on the datasets, with the labels corresponding to the discussion in Appendix D:

– ID 1: Hebb et al. (2010; discovery paper) reported 34 RV measurements obtained with the CORALIE spectrograph on the 1.2 m Euler telescope between 2008 and 2009. To the best of our knowledge and after contacting the authors of the paper, the dataset reported in the paper is in BJD$_{UTC}$. We present the data transformed to BJD$_{TDB}$;

– ID 2: Hellier et al. (2011) reported 3 RV points from the CORALIE spectrograph on the Swiss Euler 1.2 m telescope in 2009. The data were reported in BJD$_{UTC}$ in Hellier et al. (2011), so they are transformed here into BJD$_{TDB}$;

– ID 3: Hellier et al. (2011) reported 36 points during and around more than one transit in 2010 using the HARPS spectrograph on the ESO 3.6 m at La Silla, taken in order to measure the Rossiter-Mclaughlin effect. As well as for ID 2, the data were

reported in BJD$_{UTC}$ in the original paper, so they have been transformed here into BJD$_{TDB}$;

– ID 4: Albrecht et al. (2012) reported 20 data points taken in 2010 as measurements of the Rossiter-McLaughlin effect with the *Magellan* II (*Clay*) 6.5 m telescope and the Planet Finder Spectrograph (PFS);

– ID 5: Knutson et al. (2014) reported 3 RV measurements obtained with the High Resolution Echelle Spectrometer (HIRES) on the 10 m Keck I telescope between 2008 and 2013;

– IDs 6,7: Sedaghati et al. (2021) reported 88 RV points taken with VLT/ESPRESSO between 2019 and 2020, used to derive the Rossiter-McLaughlin effect and characterize the atmosphere of the planet. The two different IDs are given because of some setup changes in ESPRESSO, as described by Sedaghati et al. (2021), which lead to the introduction of a small offset. Moreover, as clarified with the first author of that paper, ID 6 was reported in BJD$_{UTC}$ in the original paper, while ID 7 in BJD$_{TDB}$, therefore the first one is transformed;

– ID 8: reported 19 RV points taken by us using the High Accuracy Radial velocity Planet Searcher (HARPS, Mayor et al. 2003) at the ESO La Silla 3.6 m telescope under the programme 0104.C-0849 (PI: Sz. Csizmadia). The observations were performed between 6 and 21 February 2020. We tried to obtain 1–3 points per night and we planned the observations to have a good phase coverage. The exposure time was 1200 s while the spectral resolution as 115 000. The *objAB* observing mode of HARPS was used, covering the 378–691 nm wavelength range. The measured signal-to-noise ratio (S/N) varied between 10.2 and 21.6 depending on weather and seeing conditions. The data were reduced by the standard HARPS pipeline available at La Silla Observatory and the results with their corresponding uncertainties are reported in Tables D.1.

All RV observations are shown in Fig. 1. As described in Sect. 5.2, the datasets have different offsets {which are subtracted in the figure. They are fitted in our model by including the term $V_{i,instr}$ in Eq. (7). As for the transit and occultation mid-times, the time unit of the observation was transformed and uniformized to BJD$_{TDB}$ when necessary.

5. Data analysis

5.1. Long-term effects in RVs

In this section, we study the long-term effects affecting the RV curve. If present, they must be identified and subtracted before

---

[2] http://var2.astro.cz/EN/tresca/index.php
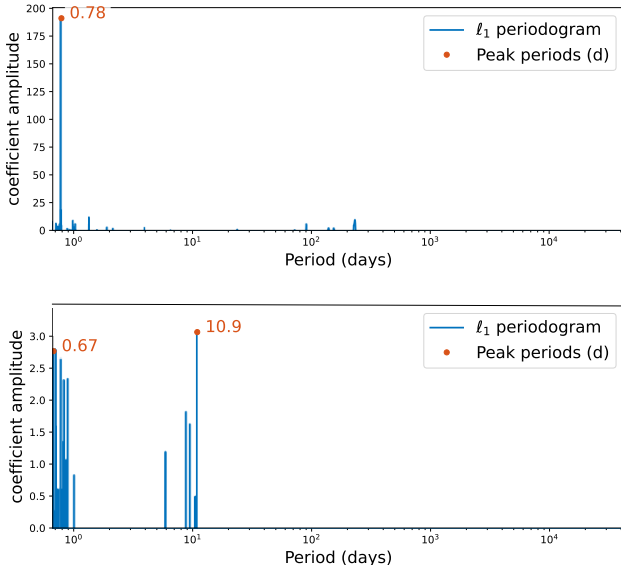
Fig. 2. l_1 periodogram of all RV data outside the transit (top). There is only one significant peak with false alarm probability $\simeq 10^{-31}$. The periodogram of the residuals after the subtraction of the contribution of planet b (bottom). All residual peaks have false alarm probabilities of >20%.

modeling and estimating the rate of periastron precession in Sect. 5.2.

First, we applied the l_1 periodogram (Hara et al. 2017) to the archive and newly acquired RV data (ID 8, see Fig. 2) to search for further companions in the system, in addition to the confirmed planet in the system. This method was developed specifically to find companions in RV datasets and can be used in a similar way to a Lomb–Scargle periodogram. To verify the significance of the peaks, we followed the re-sampling approach suggested by Hara et al. (2017): we randomly removed 10–20% of the data and re-computed the periodogram. Some peaks did not appear after the re-sampling, therefore, we did not consider them real. After the re-sampling, we identified only one peak at 0.78 d, as shown in the top plot of Fig. 2. It was retrieved in correspondence with the orbital period of WASP-19Ab, with a false alarm probability (FAP) of $\log_{10}(\mathrm{FAP}) = -30.9$ (FAP $\simeq 10^{-31}$). The analysis shows no evidence of any additional periodic signal in the RV data.

We also re-computed the periodogram on the RV residuals after the subtraction of the signal of the first planet (see bottom plot in Fig. 2). After a re-sampling of the data, only a few small peaks are left. However, their FAP is $\geqslant 0.2$, meaning that any peaks are due to artefacts.

We estimated the sensitivity of our search for perturbing bodies in the data by performing a sensitivity study based on the transit timing variations. We calculated the maximum mass of a perturber in the system as a function of the maximum amplitude of the TTVs (see Eq. (2) in Holman & Murray 2005). Our analysis shows that the maximum allowed mass of the perturber, M_c, as a function of its orbital period, P_c, assuming different values of the orbital eccentricity ($e = 0.0, 0.2, 0.4, 0.6$, and 0.8). The analysis shows that the region above 4000 $M_{\mathpzc{Ψ}}$ and period below 20 days is excluded by the TTV observations.

We also performed a sensitivity study based on the RVs. The maximum amplitude of the RV residuals after the subtraction of the signal of the orbit of planet b (with Sedaghati et al. 2021's parameters) is around 52 m s^{-1}. Through Kepler's third
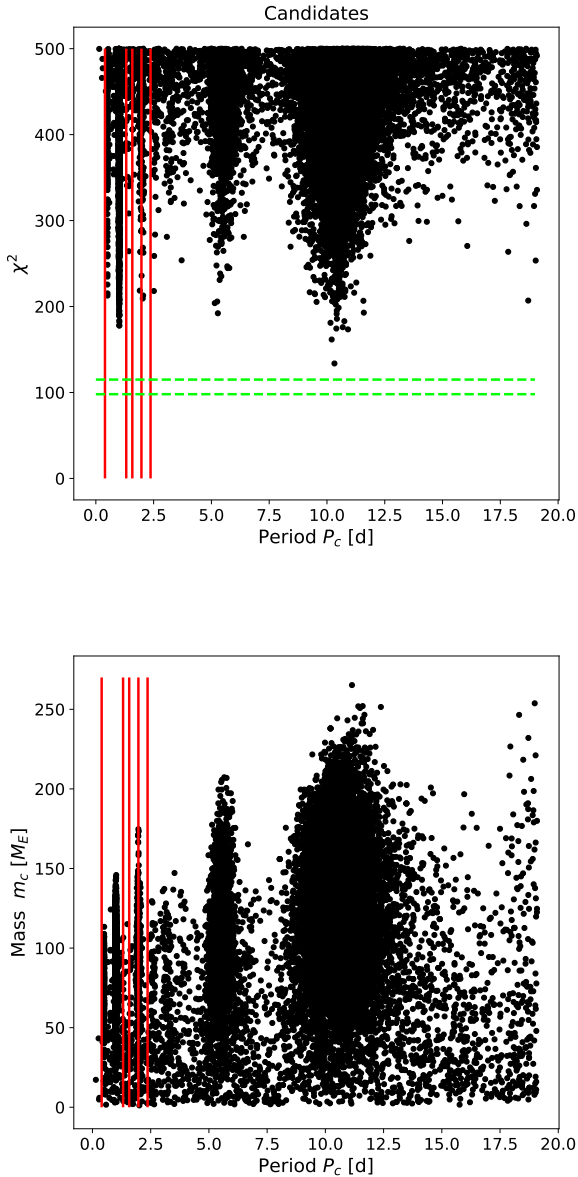
law, we estimated the maximum mass of the putative perturber. With an orbital period equal to 12 yr (the total length of the RV dataset), we obtained $M_c \simeq 3.9\ M_{\mathpzc{Ψ}}$ and an orbital distance of $\simeq 5$ AU. We fitted the data with an additional Keplerian signal (beyond the signal of planet b) mimicking a hypothetical candidate for planet c. We injected a candidate and repeated the experiment two billion times with different random eccentric orbital parameters and fitted the new HARPS RV data. We varied the candidate parameters as follows: $\sqrt{e} \cdot \sin \omega_0$ and $\sqrt{e} \cdot \cos \omega_0$ between -1.0 and 1.0, the RV semi-amplitude K_c between 0.1 and 100 m s^{-1} (to widely investigate the amplitude of the RV residuals with errorbars) and the orbital period between 0.1 and the length of the dataset ($\simeq 19$ d for the first attempt with the only HARPS dataset and $\simeq 12$ yr for the second attempt with the whole dataset). Moreover, from Kepler's third law, we set the following condition to ensure that the orbit would not collide with the star:

$$P_c \geqslant \frac{2\pi R_\star^{3/2}}{\sqrt{GM_\star}}, \tag{6}$$

where G is the gravitational constant, while $R_\star$ and $M_\star$ are the radius and mass of the host star, respectively. With these constraints and varying the orbital parameters in the aforementioned ranges, the candidate mass range is found to be between $\simeq 1.4$ and $\simeq 400\ M_\oplus$.

The results of our simulation (see Fig. 3) suggest scenarios that satisfy the condition $\chi^2 \leqslant 500$. The top plot shows the χ^2 of the model when including the proposed perturber, corresponding to five more free parameters: transit epoch, period, RV semi-amplitude, $\sqrt{e} \cdot \sin \omega_0$ and $\sqrt{e} \cdot \cos \omega_0$ (plotted as a function of the orbital period). Many of these candidates are discarded because the corresponding χ^2 is too high or the amplitude of the perturbing body on the RV curve would be over a dozen m s^{-1}, so they would definitely be visible in the RV data and in the periodogram. The red lines underline the periods corresponding with the stable orbital regions present in the stability map by Cortés-Zuleta et al. (2020). Their analysis allowed for the presence of a second planet either in 1:2, 5:3, 2:1, 5:2, or 3:1 resonance with planet b, corresponding to orbital periods of 0.39 d, 1.31 d, 1.58 d, 1.97 d, or 2.37, respectively. Some of these periods correspond with regions in the figure that are densely populated by our best candidates. The bottom plot shows the mass of the candidate plotted against its orbital period. Again, we highlight the stable orbit by Cortés-Zuleta et al. (2020) with red dashed lines.

The expected χ^2 would be around the number of degrees of freedom (19 total datapoints for dataset 8, of which 15 were fitted as out-of-transit points and 11 free parameters), while the lowest χ^2 we obtained during the simulations is $\simeq 134$ (clearly visible in the top plot of Fig. 3 at $\simeq 10$ d orbital period). We fit the HARPS data with a one-planet eccentric orbit model to compare it to the scenarios with a perturbed. Without adding any RV jitter, the χ^2 of this model is $\simeq 35$. Since the two-planet model has four more free parameters, by applying the Bayesian information criterion (BIC), we found no evidence of the presence of a perturber in the system with a period within the length of the dataset with this approach. For weak (respectively, strong) evidence (see Kass & Raftery 1995 for more details) that the two-planet model is preferred, a χ^2 value below 115 (respectively, 98) is needed. We also injected a candidate in the whole RV dataset (IDs from 1 to 8), but we obtained an even higher χ^2, resulting in an even more unlikely presence of a perturbed. Our results exclude it up to an RV amplitude of $\simeq 1$ m s^{-1}.

5.2. Rate of apsidal motion

In this section, we describe the code used for the data analysis (by allowing for non-zero periastron precession) with the fitted parameters and the results.

We used the approach and idl code developed by Csizmadia et al. (2019) to analyze the RV data in parallel with mid-transit and occultation times. Since then, the code has been modified and updated. Now the Genetic Algorithm minimization is followed by a differential-evolution Markov chain Monte Carlo (DE-MCMC, Ter Braak 2006) algorithm to explore the parameter space. The values of the fitted parameters (see Table 4 for the list of such parameters) obtained by the Genetic Algorithm are used as a starting point for the DE-MCMC analysis to derive the posterior probability distributions. The Genetic Algorithm is initialized with a population set made of 200 individuals. In the DE-MCMC we run 90 chains. The first 6×10^4 steps of each chain are discarded as part of the burn-in phase. They are followed by 10^4 more DE-MCMC steps, which are used for the posterior distributions. The convergence is checked by the Gelman - Rubin test applied on the steps that follow the burn-in phase. At the end of the run, all parameters resulted in having $R < 1.2$ (Gelman & Rubin 1992).

The priors that are used on the fitted parameters are set from the results in the literature (mainly from Hellier et al. 2011) and noted in Table 4 along with the results. The prior on the eccentricity is set as the weighted mean and standard deviation of the results in the literature (Hebb et al. 2010; Anderson et al. 2010, 2013; Hellier et al. 2011; Mandell et al. 2013; Lendl et al. 2013; Zhou et al. 2014; Knutson et al. 2014). From this, the priors on $\sqrt{e} \cdot \sin \omega_0$ and $\sqrt{e} \cdot \cos \omega_0$ are calculated as a combination of the two parameters. The contribution on the χ^2 of the priors was calculated the same way as in Csizmadia et al. (2019).

We modeled the radial velocity of the host star with a Keplerian motion but with a time-variable ω:

$$V_{\mathrm{rad},i,j} = V_\gamma + V_{i,\mathrm{instr}} + K \cdot (e \cdot \cos \omega(t_j) + \cos(v_j + \omega(t_j))) + \delta V(t_j),$$
(7)

with a secular advance of the longitude of periastron, $\dot\omega = \mathrm{d}\omega/\mathrm{d}t$, caused by the tidal and rotational potential (as expressed in Eq. (A.8)):
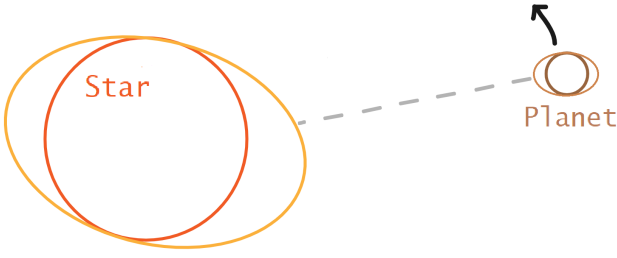
$$\omega(t_j) = \omega_0 + \dot\omega(t_j - t_0),$$
(8)

where i is the index of the instrument used and j is the index of the time when the observation was taken; V_γ is the systematic velocity of the barycenter of WASP-19Ab system relative to the barycenter of the Solar System. Different datasets may have different instrumental zero-point offsets, $V_{i,\mathrm{instr}}$. Finally, K is the radial velocity half-amplitude:

$$K = \frac{2\pi a_\star \sin i}{P_a \sqrt{1 - e^2}}.$$
(9)

In this expression, $a_\star$ is the semi-major axis of the star around the common center of mass and i is the inclination between the orbital plane and the plane of the sky (perpendicular to the line of sight).

Here, δV is the non-orbital apparent contribution that arises from the rotation of the star around its own axis. The stellar and planetary shapes are distorted ellipsoids with the longest axis in the direction of the radius vector connecting them, as shown in Fig. 4. Their apparent area varies continuously during an orbital revolution, therefore the emitted light changes (i.e., the

Fig. 3. Properties of third bodies excluded by RV data. The plot shows the results for the simulated scenarios including a putative companion planet c of different masses at different periods. Each black dot represents one of the around 20 000 selected scenarios (see the text for more details). Top plot: χ^2 value vs the orbital period of the perturber. The red lines correspond to the period of the stable orbits predicted by Cortés-Zuleta et al. (2020). The two horizontal dashed lines represent the χ^2 required to have weak (upper line) or strong (lower line) evidence of a second planet, as discussed in the text. Bottom plot: mass and orbital period of the selected candidates.

This simulation confirms the conclusion of Knutson et al. (2014) when looking for the acceleration of the system due to possible long-period companions. The cited paper does not find an acceleration that differs from zero by more than 3σ. In this way, we extended the orbital period range of investigation in Knutson et al. (2014) from between 0 and 1702 d up to $\simeq 4200$ d.

Since we did not find any additional companion and there is no evidence for long-term trends in the data, we proceeded with our analysis by introducing periastron precession in the fit.

Fig. 4. Star-planet system geometry when tidal interactions occur. The spherical shapes that star and the planet would have in the absence of tidal interactions are drawn in red and dark brown. The tidal bulges are drawn in orange and light brown, respectively. They arise on the stellar and planetary surfaces (respectively in orange and light brown) and rotate with the star itself and are elongated in the direction of the other body. The tidal lags are also drawn. The image is not to scale.

ellipticity effect). Moreover, in close binary systems, part of the radiation of each of the two components falls on the surface of the companion. It is absorbed and re-emitted (or scattered) in all directions, varying during the orbital phase (i.e., the reflection effect).

These two photometric effects in the RV data due to distortion are described by Kopal (1959) as a non-orbital contribution to the RV curve:

$$
\begin{aligned}
\delta V = &-\frac{3}{2} K \ \sqrt{1-e^2} \ \frac{M_\star + m_p}{M_\star} \ \frac{P_{orb}}{P_{rot,\star}} \left(\frac{R_\star}{a}\right)^4 \cdot \\
&\cdot \left(1 + \frac{k_{2,\star}}{2}\right) \sin i \cdot \sin\left(2\left(v+\omega\right)\right) f_2,
\end{aligned}
\tag{10}
$$

where the Love number of the star is assumed from theoretical calculations (we take it from Claret 2004). Then, $P_{rot,\star}$ is the rotational period of the star around its axis and f_2 takes into account the limb darkening. For more details on f_2 see Kopal (1959) and Csizmadia et al. (2019).

Arras et al. (2012) already includes such calculations for precise RV analysis of WASP-18A, but neglects the effect of stellar rotation. In other words, a synchronous rotation of the star is assumed. However, for WASP-19A this is not the case. It is known to be active, showing a rotational modulation with $P_{rot,\star}$ = 10.5 d (Hebb et al. 2010). Therefore, the term $P_{orb}/P_{rot,\star}$ is not expected to be 1, but $\simeq 0.79$ d/10.5 d $\simeq 0.08$, introducing a factor of about 12 difference in the amplitude of such effect calculated by Arras et al. (2012) and Kopal (1959). The amplitude of this contribution is around 0.19 m s^{-1}, so it is negligible for WASP-19A if compared to the typical observational error-bars. The period of this effect is linked to the sine term of the true anomaly in Eq. (10) and, therefore, it is half of the orbital period.

Moreover, we added jitter terms for each spectrograph to the RV model (see, e.g., Baluev 2009 for a discussion of instrumental jitters). The jitter is composed of an instrumental and a stellar contribution. It is not possible to separate them. As a starting point, if present, we used the values proposed by the corresponding literature. In particular, 13 m s^{-1} for Hebb et al. (2010)'s data (ID 1, as in Anderson et al. 2010), 14.1 m s^{-1} and 6.9 m s^{-1} for Coralie (ID 2) and HARPS (ID 3) Hellier et al. (2011)'s data, respectively, 20 m s^{-1} for Albrecht et al. (2012)'s (ID 4) and 17.8 m s^{-1} for Knutson et al. (2014)'s (ID 5) RVs. Then, we

refined all the jitter values by minimizing the χ^2 as:

$$
\chi^2_{jit,instr} = \sum_{i=1}^{n_{data}} \frac{(O_i - C_i)^2}{\sigma_i^2 + \sigma_{jit_{instr}}^2} = n_{data} - 1,
\tag{11}
$$

where O_i and C_i are the observed points (see Table D.1) and the (calculated) expected values from the model, respectively; σ_i represents the observed errors corresponding to O_i and n_{data} is the number of datapoints in the subset. This procedure was iteratively repeated until the condition of Eq. (11) was fulfilled. Due to the highly inhomogeneous set of data, this procedure allows for every RV dataset to have a weight in the fit proportional to the number of its data points.

We also added a jitter value for transits and one for occultations to account for inhomogeneities in the dataset and for a perturber with an orbital period longer than 12 yr, as described in Sect. 5.1. The fitted values for the jitter terms can be found in Table 4, along with all the fitted and derived parameters in our model.

The orbital eccentricity is a key issue for Love number studies: in circular orbits, apsidal motion is not observable. In addition, the argument of periastron is hard to measure if eccentricity is not well known. When the eccentricity is small, then its uncertainty range is often large and the investigators find that the orbit is compatible with a circular one. However, such results in the literature do not necessarily imply that the orbit is circular, despite many investigators setting a zero eccentricity (and not propagating the error bars of eccentricity to the corresponding result). It only means that an upper limit exists for eccentricity.

Moreover, a certain dataset may indicate the presence of an eccentric orbit with an accurate result. However, the sample size is not big enough or not aptly distributed to get the uncertainty ranges accurate enough. The results are imprecise and the real value of eccentricity is vague.

Although we collected more RV and TTV data than any previous study of the WASP-19Ab system, the datasets come from various instruments with different precisions and, thus, are non-homogeneous. The value of eccentricity may be affected by the different data accuracy, as some of the data sets are diluted by less precise measurement points. Because of these reasons, any previous estimate of eccentricity can be accurate but imprecise.

Applying a prior on the eccentricity in the fitting procedure can be a valid approach. The average and standard deviation of the previously reported eccentricities can better represent reality than any single determination from a limited dataset. Therefore, we calculated the weighted average of the previous eccentricity measurement and their weighted standard error using their uncertainty range as weights. Therefore, we performed a fit using this mean eccentricity as a prior with their weighted standard error as a Gaussian width.

In addition, in the calculation of the χ^2 of the fit, priors also on the stellar temperature, $T_{eff,\star}$, and Love number, $k_{2,\star}$, the mass ratio, q, the orbital inclination, i, the orbital over rotational period ratio, $F_\star$, and the ratio, $r_p/R_\star$, were added as described in Csizmadia et al. (2019).

Together with the RVs, we modeled mid-transit and mid-occultation times listed in Tables C.1–C.2 mainly to refine the determination of the first transit epoch and the period. To include periastron precession in the fit of predicted mid-times, we followed the approach of Gimenez & Garcia-Pelayo (1983) and Csizmadia et al. (2019).

Table 4. Parameters of the WASP-19Ab system.

Parameter		Symbol	Fit	Value	Priors
Assumed parameters					
Stellar rotation		$V\sin(i)$		4.63 km s^{-1} [†]	
Stellar mass		$M_\star$		0.970 $M_\odot$	
Planet-to-star radius ratio		$r_{\rm p}/R_\star$		0.14248	
Semi-major axis		a		0.01655 AU	
First transit epoch		T_0		2 454 775.3372 BJD$_{\rm TDB}$	
Adjusted parameters					
Jitters	ID 1	jit$_1$	RVs	13.5 m s^{-1}	
	ID 2	jit$_2$	RVs	35.0 m s^{-1}	
	ID 3	jit$_3$	RVs	9.8 m s^{-1}	
	ID 4	jit$_4$	RVs	11.5 m s^{-1}	
	ID 5	jit$_5$	RVs	30.4 m s^{-1}	
	ID 6	jit$_6$	RVs	13.1 m s^{-1}	
	ID 7	jit$_7$	RVs	9.8 m s^{-1}	
	ID 8	jit$_8$	RVs	22.3 m s^{-1}	
	Transits	jit$_{\rm tr}$	Tr	0.00005 d	
	Occultations	jit$_{\rm occ}$	Occ	0.0001 d	
Fitted parameters					
Offset velocity of the system		V_γ	RVs	(20.7791 ± 0.0060) km s^{-1}	$\mathcal{U}[-\infty,+\infty]$
RV semi-amplitude		K	RVs	(253.48 ± 3.87) m s^{-1}	$\mathcal{U}[-\infty,+\infty]$
Offset instrumental velocity	ID 2	$V_{\rm instr,2}$	RVs	(0.0258 ± 0.0071) km s^{-1}	$\mathcal{U}[-\infty,+\infty]$
	ID 3	$V_{\rm instr,3}$	RVs	(0.0221 ± 0.0074) km s^{-1}	$\mathcal{U}[-\infty,+\infty]$
	ID 4	$V_{\rm instr,4}$	RVs	(-20.827 ± 0.016) km s^{-1}	$\mathcal{U}[-\infty,+\infty]$
	ID 5	$V_{\rm instr,5}$	RVs	(-20.712 ± 0.014) km s^{-1}	$\mathcal{U}[-\infty,+\infty]$
	ID 6	$V_{\rm instr,6}$	RVs	(-0.0919 ± 0.0092) km s^{-1}	$\mathcal{U}[-\infty,+\infty]$
	ID 7	$V_{\rm instr,7}$	RVs	(-0.1149 ± 0.0139) km s^{-1}	$\mathcal{U}[-\infty,+\infty]$
	ID 8	$V_{\rm instr,8}$	RVs	(0.0750 ± 0.0090) km s^{-1}	$\mathcal{U}[-\infty,+\infty]$
Anomalistic period		$P_{\rm a}$	RVs and Tr/Occ	$(0.788951\,^{+0.000012}_{-0.000017})$ d	$\mathcal{U}[-\infty,+\infty]$
		$\sqrt{e}\cdot\sin\omega_0$	RVs and Tr/Occ	$0.03920\,^{+0.00458}_{-0.00682}$	$\mathcal{U}[-1,+1]$
		$\sqrt{e}\cdot\cos\omega_0$	RVs and Tr/Occ	$-0.00056\,^{+0.01385}_{-0.01717}$	$\mathcal{U}[-1,+1]$
Periastron precession rate		$\mathrm{d}\omega/\mathrm{d}t$	RVs and Tr/Occ	$(0.065\,^{+0.007}_{-0.010})^\circ$ d^{-1} =	
				$(233\,^{+25}_{-35})''$ d^{-1}	$\mathcal{U}[-\infty,+\infty]$
Stellar Love number		$k_{2,\star}$	RVs	0.0200 ± 0.0069	$\mathcal{N}(0.02;0.004)$
Stellar temperature		$T_{\rm eff,\star}$	RVs	(5498.65 ± 172.86) K	$\mathcal{N}(5500\,{\rm K};100\,{\rm K})$
Planet-to-star mass ratio		$q = m_{\rm p}/M_\star$	RVs	0.001150 ± 0.000057	$\mathcal{N}(0.00115;3.3\cdot10^{-5})$
Stellar radius over semi-major axis		$R_\star/a$	RVs	0.2785 ± 0.0070	$\mathcal{N}(0.2784;0.0040)$
Orbital-to-rotational stellar period		$F_\star = P_{\rm orb}/P_{\rm rot,\star}$	RVs	0.0729 ± 0.0074	$\mathcal{N}(0.0729;0.0043)$
Orbital inclination		i	RVs and Tr/Occ	$(79.40 \pm 0.69)^\circ$	$\mathcal{N}(79.4;0.4)$
Derived parameters					
Eccentricity		e		$0.00172\,^{+0.00035}_{-0.00033}$	
Periastron angle		ω_0		$(89.71\,^{+24.68}_{-19.12})^\circ$	
Sidereal period		P_s		$(0.788839267\,^{+0.000000018}_{-0.000000019})$ d	
Planetary Love number		$k_{2,\rm p}$		$0.20\,^{+0.02}_{-0.03}$	

Notes. Assumed, adjusted – according to Eq. (11) – fitted parameters and their priors, and derived parameters for our model which fits RVs and transit/occultation mid-times in parallel. The third column indicates if the parameter was fitted to model radial velocity ("RV") and/or mid-transit and mid-occultation times ("Tr/Occ"). The last column shows the results of our analysis. The offset related to ID 1 ($V_{\rm instr,1}$) was not included because the first dataset was used to derive the relative velocity between the observer and the center of mass of the system ($V_{\rm gamma}$). The solutions are calculated only from those steps of the DE-MCMC that fall within the distribution around the highest peak of the posterior distribution of $\dot{\omega}$ (see Fig. 6, solution B). Errorbars are given with 1σ confidence level. The reported values and errorbars of the sidereal period P_s, ω_0 and e are not calculated – as $P_s = P_a \cdot (1 - P_a \cdot \dot{\omega}/n)$, $\arctan(\sqrt{e}\cdot\sin\omega_0/\sqrt{e}\cdot\cos\omega_0)$ and $(\sqrt{e}\cdot\sin\omega_0)^2 + (\sqrt{e}\cdot\cos\omega_0)^2$ respectively – from the reported values of P_a, $\dot{\omega}$, $\sqrt{e}\cdot\sin\omega_0$ and $\sqrt{e}\cdot\cos\omega_0$ but from the median of the distribution resulting from the combination of the posterior distributions of $\sqrt{e}\cdot\sin\omega_0$ and $\sqrt{e}\cdot\cos\omega_0$. [†]Hellier et al. (2011).
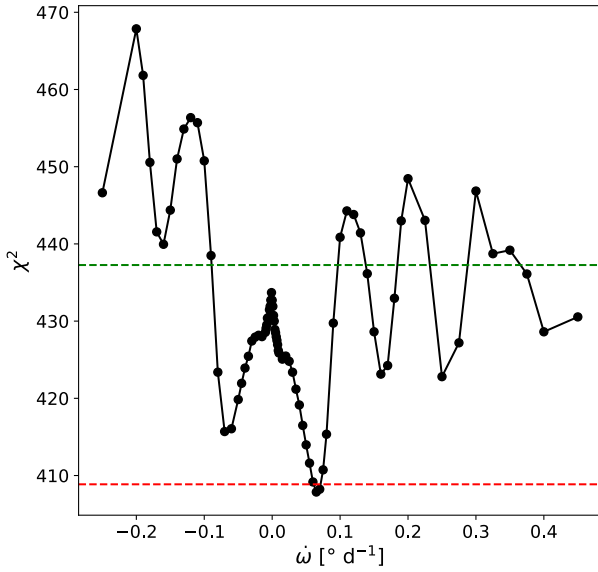
Fig. 5. χ^2 values of the fit when varying $\dot{\omega}$ in the model. The horizontal dashed line separates the statistically worse models (over the line) from the best models (below the dashed lines). The models below the dashed lines are statistically equivalent within 1σ (68% confidence level for the red line) and 2σ (95% confidence level for the green line). Note: the significantly larger χ^2 at $\dot{\omega} = 0$. The high amount of local minima is an indication of the complexity of the problem.

5.3. Presence of apsidal motion

Because of the large parameter correlations between the mean motion and periastron precession rate (see Csizmadia et al. 2019), as a first analysis, we calculated 80 different models with fixed values of $\dot{\omega}$, the so-called semi-grid analysis. This procedure also helps to get an initial range for the fitted value of $\dot{\omega}$. The limiting values were $\dot{\omega} = -0.25$ and $+0.45°\mathrm{d}^{-1}$. We also fixed the epoch to $2\,454\,775.3372\ \mathrm{BJD}_{\mathrm{TDB}}$, while all other parameters were free in the DE-MCMC analysis. The result is presented in Fig. 5, showing the assumed value of the periastron precession rate and the corresponding χ^2 of the fit. The figure clearly shows that the joint fit of the RV and TTV data is significantly worse if $\dot{\omega} = 0$, namely, no periastron precession is present. A small amount of periastron precession improves the quality of the fit significantly. The figure shows that small negative periastron precession rates also improve the fit but still result in a statistically worse fit than the small positive precession values. From that figure and the statistical analysis, we conclude that small positive periastron precession rates are needed to have a good fit of the joint RV and TTV data of WASP-19Ab, and we are able to give a lower and an upper limit of $0.06 \lesssim \dot{\omega} \lesssim 0.075°\mathrm{d}^{-1}$. The result is refined in the next section.

6. Discussion of the results

6.1. Apsidal motion rate

In this section, we show and discuss the results of the analysis performed with the model described in Sect. 5. Contrarily to the semi-grid method (Sect. 5.3), here we fit $\dot{\omega}$ along with the other parameters.

During the analysis, we noticed that different DE-MCMC chains converged to different values of $\dot{\omega}$. In particular, as it is
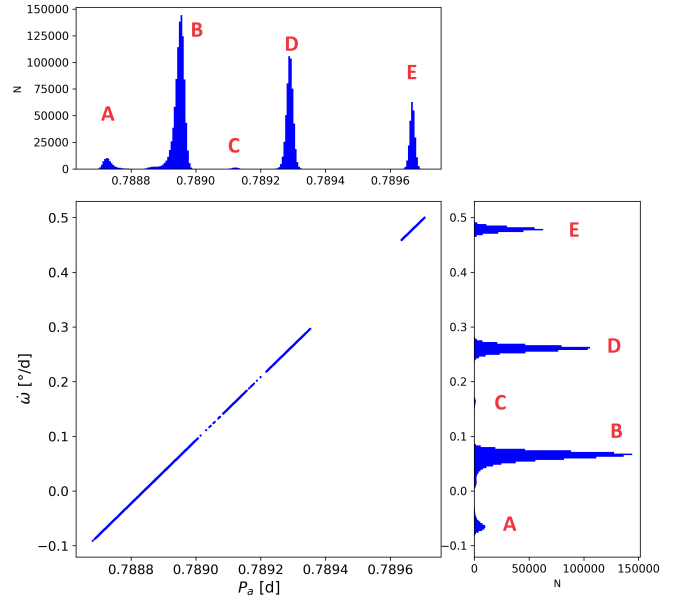
Fig. 6. Posterior distributions and correlation between the anomalistic period and periastron precession rate where the chains converged. The middle plot shows the strong correlation between these two free parameters, as in Eq. (12). On the sides, are the corresponding histograms of the posterior distributions. As can be seen from the histograms on the sides, many chains converged to various positive and negative peaks, as predicted by the semi-grid method and reported in Table 5.

Table 5. Median values of the five posterior distributions shown in Fig. 6 and corresponding χ^2 (calculated before introducing the contribution of the jitters to the uncertainty, as in Eq. (11)).

| Solution	$\dot{\omega}\ [°d^{-1}]$	χ^2
A	-0.064	416
B	$+0.065$	408
C	$+0.163$	423
D	$+0.261$	424
E	$+0.479$	430

shown in Fig. 6 and in Table 5, during the run multiple chains explored various positive and negative values of $\dot{\omega}$. Figure 6 clearly shows also the correlation between the anomalistic period and the periastron precession rate, as discussed in Csizmadia et al. (2019). It is due to the formula that links the anomalistic period P_a and the sidereal period P_s:

$$P_s = P_a(1 - \dot{\omega}/n). \qquad (12)$$

This formula that links the two quantities gives a between period and periastron precession rate, but no unique solution. The added value of including transit and occultation mid-times lies in the fact that they constrain the sidereal period, and therefore a range of values for P_a and $\dot{\omega}$ (as shown in Fig. 6), while avoiding some other ranges.

A different chain convergence shows why it was important to run various chains. Only one chain would have converged to one of the possible values, excluding the other results or could have been trapped in a local minimum (the same local minima found by the semi-grid method approach; see Fig. 5).

The highest peak of $\dot{\omega}$ (solution B) in the posterior distribution results around approximately $+0.065°\mathrm{d}^{-1}$ (summarized in
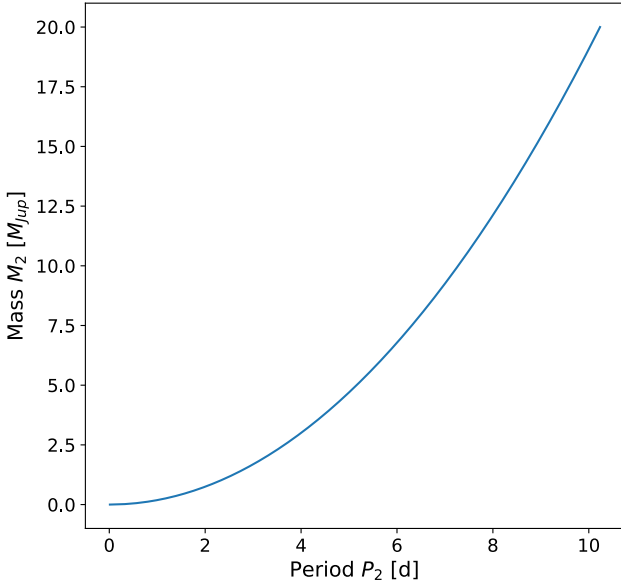
Fig. 7. Mass and orbital period of a second body that would cause a negative periastron precession rate of approximately $-0.0638°\mathrm{d}^{-1}$ (corresponding to the negative solution of the DE-MCMC analysis) on planet b, as deduced from Borkovits et al. (2011). See text for more details.

Fig. 8. Residuals of the periastron precession fit for transits and occultation mid-times, calculated with the sidereal period. Transit mid-times are plotted as blue circles, occultation mid-times as red circles. The errorbars include the jitters, as in Table 4.

Fig. 9. Data with errorbars, phase-folded with our fit including periastron precession, shown in the upper plot. The colours represent different datasets, as in Fig. 1 (see also Sect. 4.2 for more details). Residuals of the periastron precession rate fit are shown in the lower plot. The errorbars include the jitters, as in Table 4. In both plots, the in-transit points are not shown as they were not used in the fit.
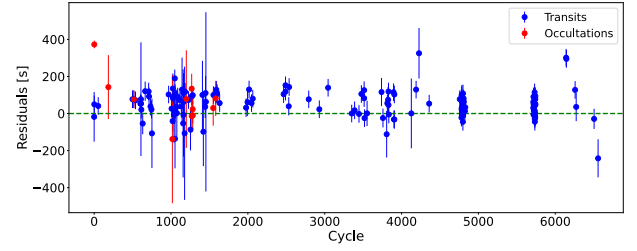
Table 5). The positive solutions C, D, and E can be discarded because of their high χ^2 values. Moreover, solution E would lead to a planetary Love number higher than 1.5, which is unphysical.

The negative periastron precession rate (solution A) would correspond either to a retrograde orbit (of the planet with respect to the rotation of the star) or to an unseen perturber. The retrograde orbit can be excluded from Rossiter-McLaughlin effect studies and TESS light curves (Wong et al. 2020). They confirm that the spin axis of the star is almost perpendicular to the orbital plane.
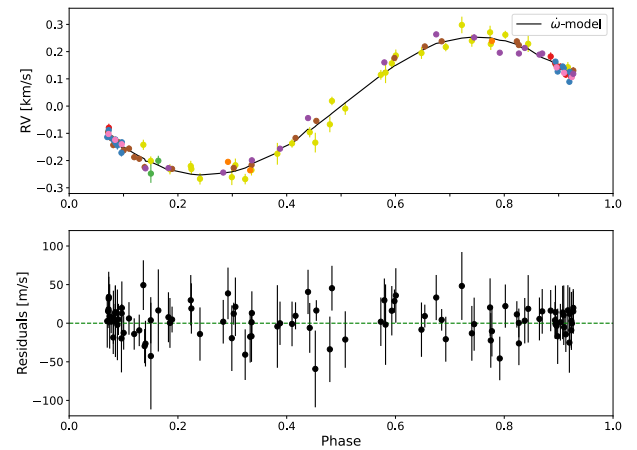
We investigated in detail the presence of a perturber in Sect. 5.1 and no evidence is found. Assuming a negative periastron precession amplitude as observed of approximately $-0.064°\mathrm{d}^{-1} = -229.68''\mathrm{d}^{-1}$, through Eqs. (12) and (16) in Borkovits et al. (2011), we can estimate the period of the body producing such a precession rate. We subtracted the general relativity contribution (calculated in Sect. 5.2 as $2.85''\,\mathrm{d}^{-1}$) from these solutions and derived the orbital period of the perturber producing such an $\dot{\omega}$. For a circular orbit, a body with a mass in the range $0.1\,M_\oplus$ and $20\,M_{2\!\!\!l}$ would have an orbital period below 10 d, as shown in Fig. 7. Such a planet would be retrievable in the RV data, while no long-term (over a 10-day orbital period) companion in this mass range can produce a negative periastron precession. Therefore the solutions yielding negative $\dot{\omega}$ values can be discarded.

The results for the fitted parameters of the $\dot{\omega}$-positive solution (solution B) with lowest χ^2 are shown in Table 4, along with their errorbars. With 99 RV points (outside the transit, 203 in total), 162 mid-transit and 11 mid-occultation points, and 19 free parameters, the reduced χ^2 is 1.02. The observed value of the total contribution $\dot{\omega}$ from the DE-MCMC analysis of the data is $(233^{+25}_{-35})''\mathrm{d}^{-1}$ (see Table 4), corresponding to an apsidal motion period of $U = 2\pi/\dot{\omega} \simeq 15$ yr.

Figure 8 shows the residuals of the transit and occultation mid-times with such a fit. Figure 9 shows the phase-folded RV curve and the residuals of our periastron precession fit.

We subtract the General Relativity term and the tidal and rotational components relative to the star from the observed $\dot{\omega}$. What is left in Eq. (1) are the tidal and rotational components due to the planet. They are related to the interior of the planet and show clearly the dependence on Love number (see Eqs. (4) and (4)). Then, $k_{2,\mathrm{p}}$ can then be estimated by inverting these equations.

The only unknown parameter is the rotational period $P_{\mathrm{rot,p}}$ of the planet itself. Since there is no measurement of the rotational period of the planet, we can only assume a value for $P_{\mathrm{rot,p}}$. The two extreme cases are presented when:

– tidal forces lead to the disruption of the planet ($P_{\mathrm{rot,p}} = 0.14$ d), then we obtain $k_{2,\mathrm{p}} = 0.07$;
– the planet is non-rotating ($P_{\mathrm{orb}}/P_{\mathrm{rot,p}} \to 0$), then we obtain $k_{2,\mathrm{p}} = 0.22$.

The measured Love number of the planet must lie in between these two values. We can suppose that tidal forces synchronize the orbital and rotational periods quite fast. This means that $P_{\mathrm{orb}} = P_{\mathrm{rot,p}}$. We can then derive $k_{2,\mathrm{p}}$ from Eqs. (A.2) and (A.7): $k_{2,\mathrm{p}} = 0.20^{+0.02}_{-0.03}$, with a precision of 15%.

For comparison, the most up-to-date values of the tidal Love number for planets and satellites in the Solar System and exoplanets are listed in Table 6. The value obtained for the fluid Love number of WASP-19Ab has the same order of magnitude as the other values derived for exoplanets.

Table 6. Fluid and tidal Love numbers measured for Solar System planets and minor bodies and exoplanets.

Body	Fluid Love number $k_{2,p}$	Method	Reference
WASP-19Ab	$0.20^{+0.02}_{-0.03}$	RVs and TTVs: periastron precession	This work
WASP-18Ab	$0.62^{+0.55}_{-0.19}$	RVs and TTVs: periastron precession	Csizmadia et al. (2019)
WASP-103b[†]	$0.59^{+0.23}_{-0.27}$	LCs: shape deformation	Barros et al. (2022)
WASP-121b[†]	$0.39^{+0.71}_{-0.81}$	LCs: shape deformation	Hellard et al. (2020)
Jupiter	0.565 ± 0.006	Juno: Doppler shift measurements	Durante et al. (2020)
Saturn	0.390 ± 0.024	Cassini: gravitational perturbations on Enceladus, Tethys, Dione and Rhea	Lainey et al. (2017)
Enceladus	0.9896 ± 0.0103	Cassini: quadrupole gravity field and its hemispherical asymmetry	Taubner et al. (2016)
Neptune	0.392	Orbital perturbations on Triton and Nereid	Jacobson (2009)

Body	Tidal Love number	Method	Reference
HAT-P-13b	$0.31^{+0.08}_{-0.05}$	RVs and TTVs: $\dot{e}$ and $\dot{\omega}$	Buhler et al. (2016)
" "	0.81 ± 0.10	RVs and TTVs: $\dot{e}$ and $\dot{\omega}$	Hardy et al. (2017)
Mercury	0.53 ± 0.03	MESSENGER: topography	Konopliv et al. (2020)
Venus	0.295 ± 0.066	*Magellan* and Pioneer Venus Orbiter: Doppler tracking	Konopliv & Yoder (1996)
Moon	0.02416 ± 0.00022	GRAIL and LLR: mapping of the gravitational field	Williams et al. (2014)
Mars	0.183 ± 0.009	Mars Express: Doppler tracking and characterization of the orbits of Phobos and Deimos	Jacobson & Lainey (2014)
Titan	0.637 ± 0.112	Cassini: response to Saturn's variable tidal field	Iess et al. (2012)

Notes. In the first half of the table, we show fluid Love numbers, which are comparable with our result. In the second half, we report tidal Love numbers. They refer to different quantities, so they are not comparable, except at longer periods when elastic stresses relax. [†]Calculated from h_2 assuming hydrostatic equilibrium.

The lower the value, the more matter is condensed toward the center of the body. The low Love number obtained, $k_{2,p} = 0.20$, is an indication of a high-mass core. This has to be tested and verified with simulations of planetary interior structure through the equations of state, however, this is beyond the scope of this paper.

Moreover, if hydrostatic equilibrium is assumed (whereby the surface of the body can be described as an equipotential surface of the tidal and rotational potentials), the second-order fluid Love number h_{2p} can also be calculated. This assumption is close to reality if the body is a giant gaseous planet. In this case, $h_{2,p} = k_{2,p}+1$ (Munk & MacDonald 1960), therefore $h_{2,p} = 1.20$ for synchronous rotation. This causes a small-shaped deformation that can be hard to observe photometrically (Hellard et al. 2019).

During the analysis, we noticed that the main contribution to the uncertainty of the fit is related to the transit fit. It is due to underestimated errorbars on the mid-transit times, which compromise the reliability of the results, increasing the χ^2 of the fit. This was already suggested by Mancini et al. (2013) regarding the 54 transits they analysed. Therefore, we increased the errorbars to 0.0005 d (approximately 43 s) if the reported uncertainties were lower than this threshold.

We also underline the importance of acquiring new light curves. Precise transit and, mostly, occultation mid-times are needed to break the degeneracy between periastron precession and the change of orbital period due to for instance companions or orbital decay.

6.2. Alternative explanations

We investigated alternative scenarios to the presence of periastron precession. In particular, we searched for distant massive companions with the approach of Knutson et al. (2014). The long-term acceleration of the system was fitted by adding a γ acceleration to the RV Eq. (7) as:

$$V_{acc}(t_j) = \dot{V}_\gamma \cdot (t_j - t_0). \tag{13}$$

We ran the DE-MCMC algorithm in the case of a circular and an eccentric orbit. The posterior distribution of $\dot{V}_\gamma$ has median of $(7.37 \pm 5.02) \times 10^{-7}$ m s^{-2} for the circular case and $(7.43 \pm 4.89) \times 10^{-7}$ m s^{-2} for the eccentric one. Both results are compatible with zero and reproduce the results of Knutson et al. (2014) of $(7.52 \pm 3.94) \times 10^{-7}$ m s^{-2}. Our results increase the confidence level of a non-detection of long-term acceleration from Knutson et al. (2014)'s 1.9–1.5σ.

We also investigated the tidal decay scenario, as it has been analysed and confirmed in the system WASP-12b (see respectively Patra et al. 2017; Yee et al. 2020; Turner et al. 2021; Wong et al. 2022). The observed TTVs can be due to tidal decay or periastron precession. We fitted the RV semi-amplitude K in Eq. (9) as a time-varying parameter:

$$K(t_j) = K_0 + \dot{K}(t_j - t_0). \tag{14}$$

Deriving Kepler's laws with respect to time, we can see that a change in the RV semi-amplitude results in an opposite change in the semi-major axis.

For the circular orbit case, we obtained $\dot{K} = (-2.77 \pm 2.80) \times 10^{-8}$ m s^{-2} while for the eccentric case $(-2.60 \pm 2.73) \times 10^{-8}$ m s^{-2}. As Rosário et al. (2022), we did not find significant evidence of orbital decay. Both in the case of a long-term velocity and of tidal decay, the results are compatible with zero and therefore considered as constant.

7. Conclusions

In this study, we review the theory on tidal interaction, as described by Kopal (1978) and reported with modern notation. Using assumptions on the Love number of the star, based on well-established theoretical models of its evolution and interior structure, the apsidal motion rate allows us to constrain the Love number $k_{2,p}$ of the planet. We applied the results to a case study, namely, the system WASP-19Ab, by using archival mid-transit times, occultations, and radial velocity data, including previously unpublished RV observations made by HARPS. This

dataset covers twelve years in total. First, we ruled out previous claims of additional planetary companions in the system as possible perturbers in the radial velocity curve that could hide the small contribution of the periastron precession motion. Moreover, we investigated the presence of a long-term acceleration in the RV dataset and of tidal decay. Both these scenarios have been rejected with respect to being compatible with a zero trend. Then, we used a model that accounts for an eccentric orbit and apsidal motion in order to fit the data. We detected the presence of apsidal motion in the planetary orbit and linked it to the Love number of the planet. By assuming synchronous rotation for the planet, we derived $k_{2,p} = 0.20^{+0.02}_{-0.03}$.

The planetary fluid Love number is constrained in this system for the first time. There are few systems for which it has been measured. We take the opportunity to compare WASP-19Ab to them. Table 6 shows the fluid and tidal Love numbers of Solar system planets and bodies and exoplanets which are reported in the literature. The derived value of the fluid Love number $k_{2,p}$ of WASP-19Ab is on the same order of magnitude as the one of other Jupiter-like planets (WASP-4b, WASP-18Ab, WASP-103b and WASP-121b). A low value suggests the presence of a dense core in the planet, similar to the case of Saturn, Neptune, and WASP-121b. Note that the Love numbers of WASP-12b and WASP-4b (derived by Campo et al. 2011 and Bouma et al. 2019, respectively) are intentionally left out of the table. In the first case, the TTVs might be explained by tidal decay (Yee et al. 2020 and reference therein). In the second case, the presence of a second, long-period planet in the system (Turner et al. 2022) further complicates the TTV analysis. The results of Bouma et al. (2020) were discussed further by Harre & Smith (2023) in the light of this second planet, making the determination of $k_{2,p}$ uncertain.

No general conclusion on planetary physics can be drawn from this set of measured Love numbers because the sample is too small to be representative of the existing exoplanet population. We need observations of the Love number of more exoplanets.

We also characterize, for the first time, the stellar multiplicity of the system. We find a stellar companion with an apparent separation of $68''$, corresponding to a physical distance of almost 20 000 AU, from the system under analysis. However, its expected effect on the RV of WASP-19A is negligible.

References

Abe, L., Gonçalves, I., Agabi, A., et al. 2013, A&A, 553, A49
Albrecht, S., Winn, J. N., Johnson, J. A., et al. 2012, ApJ, 757, 18

Anderson, D. R., Gillon, M., Maxted, P. F. L., et al. 2010, A&A, 513, L3
Anderson, D. R., Smith, A. M. S., Madhusudhan, N., et al. 2013, MNRAS, 430, 3422
Arras, P., Burkart, J., Quataert, E., & Weinberg, N. N. 2012, MNRAS, 422, 1761
Baluev, R. V. 2009, MNRAS, 393, 969
Banerdt, W. B., Smrekar, S. E., Banfield, D., et al. 2020, Nat. Geosci., 13, 183
Barros, S. C. C., Akinsanmi, B., Boué, G., et al. 2022, A&A, 657, A52
Batygin, K., Bodenheimer, P., & Laughlin, G. 2009, ApJ, 704, L49
Baumeister, P., Padovan, S., Tosi, N., et al. 2020, ApJ, 889, 42
Bean, J. L., Désert, J.-M., Seifahrt, A., et al. 2013, ApJ, 771, 108
Becker, J. C., & Batygin, K. 2013, ApJ, 778, 100
Borkovits, T., Csizmadia, S., Forgács-Dajka, E., & Hegedüs, T. 2011, A&A, 528, A53
Boss, A. P. 1997, Science, 276, 1836
Bouma, L. G., Winn, J. N., Baxter, C., et al. 2019, AJ, 157, 217
Bouma, L. G., Winn, J. N., Howard, A. W., et al. 2020, ApJ, 893, L29
Buhler, P. B., Knutson, H. A., Batygin, K., et al. 2016, ApJ, 821, 26
Burton, J. R., Watson, C. A., Littlefair, S. P., et al. 2012, ApJS, 201, 36
Campo, C. J., Harrington, J., Hardy, R. A., et al. 2011, ApJ, 727, 125
Claret, A. 2004, A&A, 424, 919
Cortés-Zuleta, P., Rojo, P., Wang, S., et al. 2020, A&A, 636, A98
Csizmadia, S. 2020, MNRAS, 496, 4442
Csizmadia, S., Hellard, H., & Smith, A. M. S. 2019, A&A, 623, A45
Damasso, M., Bonomo, A. S., Astudillo-Defru, N., et al. 2018, A&A, 615, A69
Dorn, C., Khan, A., Heng, K., et al. 2015, A&A, 577, A83
Dragomir, D., Kane, S. R., Pilyavsky, G., et al. 2011, AJ, 142, 115
Durante, D., Parisi, M., Serra, D., et al. 2020, Geophys. Res. Lett., 47, e86572
Eastman, J., Siverd, R., & Gaudi, B. S. 2010, PASP, 122, 935
Ebr, J., Janeček, P., Prouza, M., et al. 2014, Rev. Mex. Astron. Astrofis. Conf. Ser., 45, 114
Efroimsky, M., & Makarov, V. V. 2013, ApJ, 764, 26
Einstein, A. 1915, Sitzungsberichte der Königlich Preußischen Akademie der Wissenschaften (Berlin), 831
Espinoza, N., Rackham, B. V., Jordán, A., et al. 2019, MNRAS, 482, 2065
Gaia Collaboration (Prusti, T., et al.) 2016, A&A, 595, A1
Gaia Collaboration (Vallenari, A., et al.) 2023, A&A, 674, A1
Gelman, A., & Rubin, D. B. 1992, Statist Sci., 7, 457
Gibson, N. P., Aigrain, S., Pollacco, D. L., et al. 2010, MNRAS, 404, L114
Gimenez, A., & Garcia-Pelayo, J. M. 1983, Ap&SS, 92, 203
Hara, N. C., Boué, G., Laskar, J., & Correia, A. C. M. 2017, MNRAS, 464, 1220
Hardy, R. A., Harrington, J., Hardin, M. R., et al. 2017, ApJ, 836, 143
Harre, J.-V., & Smith, A. M. S. 2023, Universe, 9, 12, 506
Hebb, L., Collier-Cameron, A., Triaud, A. H. M. J., et al. 2010, ApJ, 708, 224
Hellard, H., Csizmadia, S., Padovan, S., et al. 2019, ApJ, 878, 119
Hellard, H., Csizmadia, S., Padovan, S., Sohl, F., & Rauer, H. 2020, ApJ, 889, 66
Hellier, C., Anderson, D. R., Collier-Cameron, A., et al. 2011, ApJ, 730, L31
Holman, M. J., & Murray, N. W. 2005, Science, 307, 1288
Huitson, C. M., Sing, D. K., Pont, F., et al. 2013, MNRAS, 434, 3252
Iess, L., Jacobson, R. A., Ducci, M., et al. 2012, Science, 337, 457
Ivshina, E. S., & Winn, J. N. 2022, ApJS, 259, 62
Jackson, B., Greenberg, R., & Barnes, R. 2008, ApJ, 678, 1396
Jacobson, R. A. 2009, AJ, 137, 4322
Jacobson, R. A., & Lainey, V. 2014, Planet. Space Sci., 102, 35
Kass, R. E., & Raftery, A. E. 1995, J. Am. Statist. Assoc., 90, 773
Kaula, W. M. 1964, Rev. Geophys. Space Phys., 2, 661
Knutson, H. A., Fulton, B. J., Montet, B. T., et al. 2014, ApJ, 785, 126
Konopliv, A. S., & Yoder, C. F. 1996, Geophys. Res. Lett., 23, 1857
Konopliv, A. S., Park, R. S., & Ermakov, A. I. 2020, Icarus, 335, 113386
Kopal, Z. 1959, Close Binary Systems (The International Astrophysics Series, London: Chapman & Hall)
Kopal, Z. 1978, Dynamics of Close Binary Systems (Astrophysics and Space Science Library, Dordrecht: Reidel)
Lainey, V., Jacobson, R. A., Tajeddine, R., et al. 2017, Icarus, 281, 286
Lendl, M., Gillon, M., Queloz, D., et al. 2013, A&A, 552, A2
Love, A. E. H. 1911, Some Problems of Geodynamics (Cambridge: Cambridge University Press)
Mancini, L., Ciceri, S., Chen, G., et al. 2013, MNRAS, 436, 2
Mandell, A. M., Haynes, K., Sinukoff, E., et al. 2013, ApJ, 779, 128
Mayor, M., Pepe, F., Queloz, D., et al. 2003, The Messenger, 114, 20
Munk, W. H., & MacDonald, G. J. F. 1960, The Rotation of the Earth; a Geophysical Discussion (Cambridge: Cambridge University Press)
Patra, K. C., Winn, J. N., Holman, M. J., et al. 2017, AJ, 154, 4
Patra, K. C., Winn, J. N., Holman, M. J., et al. 2020, AJ, 159, 150
Pecaut, M. J., & Mamajek, E. E. 2013, ApJS, 208, 9

Petrucci, R., Jofré, E., Gómez Maqueo Chew, Y., et al. 2020, MNRAS, 491, 1243

Poddaný, S., Brát, L., & Pejcha, O. 2010, New A, 15, 297

Pollack, J. B., Hubickyj, O., Bodenheimer, P., et al. 1996, Icarus, 124, 62

Ragozzine, D., & Wolf, A. S. 2009, ApJ, 698, 1778

Rosário, N. M., Barros, S. C. C., Demangeon, O. D. S., & Santos, N. C. 2022, A&A, 668, A114

Russell, H. N. 1928, MNRAS, 88, 641

Schneider, J. 2018, in Handbook of Exoplanets, eds. H. J. Deeg, & J. A. Belmonte (Berlin: Springer), 163

Sedaghati, E., Boffin, H. M. J., Csizmadia, S., et al. 2015, A&A, 576, L11

Sedaghati, E., Boffin, H. M. J., MacDonald, R. J., et al. 2017, Nature, 549, 238

Sedaghati, E., MacDonald, R. J., Casasayas-Barris, N., et al. 2021, MNRAS, 505, 435

Sterne, T. E. 1939, MNRAS, 99, 451

Taubner, R. S., Leitner, J. J., Firneis, M. G., & Hitzenberger, R. 2016, Origins Life Evol. Biosph., 46, 283

Ter Braak, C. J. F. 2006, Statist. Comput., 16, 239

Torres, G., Fischer, D. A., Sozzetti, A., et al. 2012, ApJ, 757, 161

Tregloan-Reed, J., Southworth, J., & Tappert, C. 2013, MNRAS, 428, 3671

Turner, J. D., Ridden-Harper, A., & Jayawardhana, R. 2021, AJ, 161, 72

Turner, J. D., Flagg, L., Ridden-Harper, A., & Jayawardhana, R. 2022, AJ, 163, 281

Valencia, D., Sasselov, D. D., & O'Connell, R. J. 2007, ApJ, 665, 1413

Van Hoolst, T., Noack, L., & Rivoldini, A. 2019, Adv. Phys. X, 4, 1630316

Wagner, F. W., Sohl, F., Hussmann, H., Grott, M., & Rauer, H. 2011, Icarus, 214, 366

Williams, J. G., Konopliv, A. S., Boggs, D. H., et al. 2014, J. Geophys. Res. Planets, 119, 1546

Wong, I., Knutson, H. A., Kataria, T., et al. 2016, ApJ, 823, 122

Wong, I., Benneke, B., Shporer, A., et al. 2020, AJ, 159, 104

Wong, I., Shporer, A., Vissapragada, S., et al. 2022, AJ, 163, 175

Yee, S. W., Winn, J. N., Knutson, H. A., et al. 2020, ApJ, 888, L5

Zacharias, N., Finch, C. T., Girard, T. M., et al. 2012, VizieR Online Data Catalog: I/322A

Zhou, G., Bayliss, D. D. R., Kedziora-Chudczer, L., et al. 2014, MNRAS, 445, 2746

Appendix A: Equations of apsidal motion
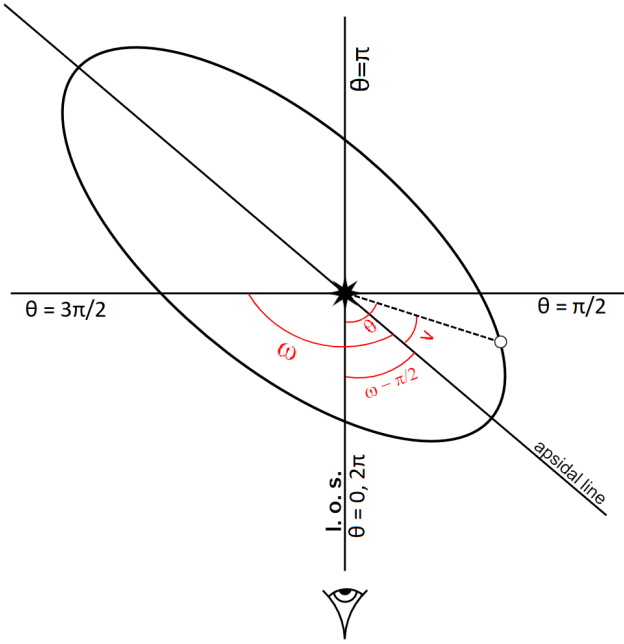
Fig. A.1. Geometry of the orbital system in the simple case of orbital inclination of $i = 90°$. The star symbol and the open dot denote the positions of the star and the planet, respectively; ω is the angle of periastron, θ is the phase from superior conjunction, and v is the true anomaly; *l.o.s.* denotes the line of sight. In this configuration, θ equals 0 for transits and π for occultations.

In this Appendix, we rewrite the equations derived by Kopal (1959, 1978) with modern notation.

First, we define the stellar and planetary disturbing accelerations $\mathbb{R}_i$ and $\mathbb{S}_i$, where the subscript i represents either the star ($i = \star$) or the planet ($i = p$). $\mathbb{R}_i$ acts in the direction of the radius vector and $\mathbb{S}_i$ in the plane of the orbit in the direction perpendicular to the radius vector and positive in the direction of motion.

The radial perturbation accelerations can be expressed as:

$$\mathbb{R}_\star = -\frac{3}{4} G(M_\star + m_p) \frac{m_p}{M_\star} k_{2,\star} \frac{R_\star^5}{r^4 \, r_{\epsilon_\star}^3} (3\cos^2 \epsilon_\star - 1), \quad (A.1)$$

and

$$\mathbb{R}_p = -\frac{3}{4} G(M_\star + m_p) \frac{M_\star}{m_p} k_{2,p} \frac{r_p^5}{r^4 \, r_{\epsilon_p}^3} (3\cos^2 \epsilon_p - 1), \quad (A.2)$$

where G is the Gravitational constant, $M_\star$ and m_p are the masses of the star and the planet, respectively, $R_\star$ and r_p their radii and $k_{2,\star}$ and $k_{2,p}$ their second-order fluid Love number.

Here, r is the radius vector:

$$r = \frac{a(1 - e^2)}{1 + e \cdot \cos v}, \quad (A.3)$$

where a is the semi-major axis of the orbit, e is the orbital eccentricity and v is the true anomaly of the planetary orbit, as shown in Fig. A.1.

A tidal lag in latitude arises if the spin axis of the two bodies is not perpendicular to the orbital plane and in general is small or even zero. On the other hand, a lag in longitude arises from asynchronism between spin and orbital rotation. The angles $\epsilon_\star$ and ϵ_p

represent the tidal lag of the star or the planet in astrocentric longitude (Efroimsky & Makarov 2013) as:

$$\epsilon_i = \frac{1}{2} \arcsin\left(-\frac{1}{Q_i} \text{sign}\left[P_{orb}/P_{rot,i} - 1\right]\right), \quad (A.4)$$

where P_{orb} is the orbital period and $P_{rot,i}$ is the rotational period of the star or the planet. The function *sign* takes the value of +1, 0 or -1, depending on the sign of the expression in the square brackets. Q_i is the tidal quality factor. A high Q factor corresponds to a weak dissipation and vice-versa (see Kaula (1964) and reference therein).

The radius vector, r_ϵ, is defined as:

$$r_{\epsilon,i} = \frac{a(1 - e^2)}{1 + e \cdot \cos(v - \epsilon_i)}. \quad (A.5)$$

The difference between r and r_{ϵ_i} is due to a finite speed of progression of the radial tidal waves in viscous matter. The amplitude of tidal distortion is not maximum when the bodies are closest to each other, but at a later time. We consider a fluid case, which corresponds to $\epsilon_i = 0$.

In addition, we define the tangential perturbation accelerations:

$$\mathbb{S}_\star = \frac{3}{4} G(M_\star + m_p) \frac{m_p}{M_\star} k_{2,\star} \frac{R_\star^5}{r^4 r_{\epsilon_\star}^3} \sin(2\epsilon_\star), \quad (A.6)$$

for the star and

$$\mathbb{S}_p = \frac{3}{4} G(M_\star + m_p) \frac{M_\star}{m_p} k_{2,p} \frac{r_p^5}{r^4 r_{\epsilon_p}^3} \sin(2\epsilon_p), \quad (A.7)$$

for the planet. Finally, $\mathbb{R} = \mathbb{R}_\star + \mathbb{R}_p$ and $\mathbb{S} = \mathbb{S}_\star + \mathbb{S}_p$.

There is a third perturbing acceleration component beyond $\mathbb{S}$ and $\mathbb{R}$. It is normal to the plane of the orbit and positive toward the north pole. However, its contribution is zero as it is proportional to the latitude component of the angle of tidal lag. It can arise only if the orbital plane is inclined with respect to the equatorial plane of the body (star or planet). We neglect this term because the Rossiter-McLaughlin measurements of WASP-19A show an equatorial orbit (see, e.g., Sedaghati et al. 2021).

With the introduction of the terms, $\mathbb{S}$ and $\mathbb{R}$, the perturbation equations can be easily written following Kopal (1959, 1978). The temporal change of the argument of periastron measured from the ascending node is:

$$\frac{d\omega}{dt} = \frac{\sqrt{1 - e^2}}{nae} \left[-\mathbb{R} \cos v + \mathbb{S} \left(1 + \frac{r}{a(1 - e^2)}\right) \sin v\right], \quad (A.8)$$

where n is the mean motion that can be defined through Kepler's law or through the orbital period P_{orb}.

Figure A.2 shows the effect of the periodical and secular perturbations on ω, as in Eq. (A.8). The plots were made setting the physical and orbital parameters to those of the exoplanetary system WASP-19Ab (see Sect. 3) with the Love number of WASP-18Ab (Csizmadia et al. 2019) as a first guess. We present how it evolves over 1, 10, 50, 100, and 500 orbits.
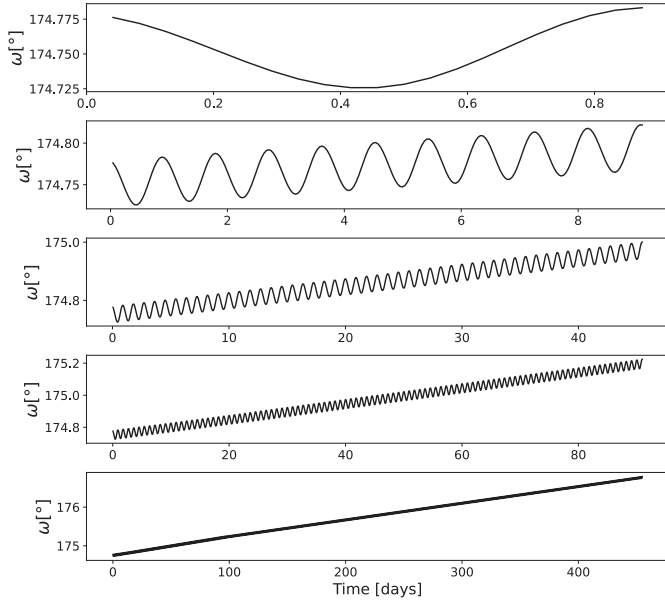
Fig. A.2. Temporal change of the osculating orbital element $\omega(t)$ due to tidal and rotational potentials, as described by Eq. (A.8), assuming the orbital properties of the system WASP-19 (see Sect. 3.1) and the Love number of WASP-18Ab Csizmadia et al. (2019).

Appendix B: Planetary eccentricity driven by WASP-19B

Here, we show that a companion star on a very eccentric orbit is able to cause an eccentric orbit of the planet in the WASP-19 system.

Borkovits et al. (2011) gave analytic expressions for the variations of the orbital elements up to the sixth order of the inner eccentricity for any arbitrary orientation of the orbits. However, we do not know the spatial orientation of the orbit of the companion star B nor the longitude of the node of the planet b. Therefore, we assume co-planar orbits for the planet and star B, and we also assume that their semi-major axes are aligned. In this specific case, the integration of Eq. (9) of Borkovits et al. (2011) gives the simple expression for the eccentricity of the planet.

$$e_b = \sqrt{\frac{e^{A_L/2 \cdot f(v_B)}}{1 + e^{A_L/2 \cdot f(v_B)}}}, \tag{B.1}$$

where $f(v_B)$ is

$$f(v_B) = \frac{1}{2}\cos 2v_B + \frac{4e_B}{3}\cos^3 v_B, \tag{B.2}$$

and, A_L,

$$A_L = \frac{15}{8}\frac{P_b}{P_B}\frac{M_B}{M_A + M_B + M_b}\frac{1}{(1 - e_B)^{3/2}}. \tag{B.3}$$

Here v_B is the true anomaly of star B and it holds the time-dependence, P and M are the orbital periods around star A and the masses of the bodies and e is the eccentricity. Indices A and B stand for stars A and B respectively, while index b denotes the planet.

The lower period limit of star B around star A can be estimated assuming that P_B is minimum if star B is in apoastron. In this case, the observed separation between stars A and B

corresponds to a distance equal to $a_B(1 + e_B)$. For different values of e_B, we can determine the semi-major axis that yields the orbital period, P_B, via Kepler's third law. In case of $e_B = 0.995$ $a_B \approx 10^4$ AU and $P_B \approx 1$ Myrs (note: the periastron point is still located at 50 AU from star A).

Since we do not know the exact orbit of star B, we just estimate the planetary eccentricity. Taking the Taylor series of the exponential function in Eq. (B.1) and neglecting the time dependence, we obtain

$$e_b \approx \sqrt{A_L/2 \times \left(\frac{1}{2} + \frac{4e_B}{3}\right)}. \tag{B.4}$$

Using the aforementioned numerical values and assuming $M_B \sim 0.4 M_\odot$, we get $e_b \approx 0.0011$. This calculation leads to an order of magnitude estimation of whether any (or a specific) combination of orbital elements can be responsible for the observed eccentricity. A deviation from this estimate can be due to the unknown spatial orientation of the different orbits.

Appendix C: Tables of transits and occultations

Table C.1. Transits found in the literature: cycle number, referred to in Hebb et al. (2010) - mid-transit point in BJD$_{TDB}$, its error, details on the observations, and reference.

Cycle number N	T$_{mid}$ [days] BJD$_{TDB}$ - 2 450 000	Uncertainty [days]	Observations	Reference
0	4775.33720	0.00150	WASP-South, 2.0m - Faulkes Telescope South (FTS)	Hebb et al. (2010)
2	4776.91566	0.00019	HAWK-I (VLT)	Anderson et al. (2010)
53	4817.14633	0.00021	2.0m - Faulkes Telescope South (FTS)	Lendl et al. (2013), from Hebb et al. (2010)
499	5168.96879	0.00009	EFOSC on NTT, WASP-South and Hebb et al. (2010)'s LCs	Hellier et al. (2011)
517	5183.167890	0.000068	IRAC on Spitzer	Anderson et al. (2013)
538	5199.73343	0.000134	0.25m - Observatorio Astronómico Beta Orionis[1]	F. Tifner (TRESCA)
604	5251.79657	0.00014	EFOSC2 on NTT	Tregloan-Reed et al. (2013)
605	5252.58544	0.00010	EFOSC2 on NTT	Tregloan-Reed et al. (2013)
609	5255.74077	0.00012	EFOSC2 on NTT	Tregloan-Reed et al. (2013)
609	5255.741050	0.000145	EFOSC on NTT	Dragomir et al. (2011), from Hellier et al. (2011)
614	5259.68459	0.000359	0.40m - Observatorio Cerro Armazones[2]	Colque (TRESCA) re-analysed by Petrucci et al. (2020)
632	5273.88282	0.00062	0.25m - Rarotonga Observatory[3]	P. Evans (TRESCA)
664	5299.12768	0.00055	0.24m - YSVP Observatory[4]	I. Curtis (TRESCA)
687	5317.27076	0.00006	ASTEP 400 Telescope	Abe et al. (2013)
709	5334.62540	0.00021	DFOSC on 1.54m - Danish Telescope	Mancini et al. (2013)
714	5338.56929	0.00023	TRAPPIST	Lendl et al. (2013)
733	5353.55659	0.00024	DFOSC on 1.54m Danish Telescope	Mancini et al. (2013)
746	5363.81131	0.00041	0.30m - MAGS Observatory[5]	G. Milne (TRESCA)
752	5368.54285	0.00212	DFOSC on 1.54m - Danish Telescope	Mancini et al. (2013)
969	5539.72329	0.00030	EulerCam on Euler-Swiss	Lendl et al. (2013)
1007	5569.69827	0.00036	TRAPPIST	Lendl et al. (2013)
1021	5580.74124	0.00058	1.0m - CTIO[8]	Dragomir et al. (2011)
1024	5583.10979	0.00089	0.24m - YSVP Observatory[4]	I. Curtis (TRESCA)
1026	5584.68693	0.00024	TRAPPIST	Lendl et al. (2013)
1026	5584.68685	0.00019	EulerCam on Euler-Swiss	Lendl et al. (2013)
1038	5594.15188	0.00168	0.30m - PEST[6]	TG Tan re-analysed by Mancini et al. (2013)
1047	5601.25164	0.00071	D0.30m - PEST[6]	TG Tan (TRESCA) re-analysed by Mancini et al. (2013)
1049	5602.83138	0.00046	TRAPPIST	Lendl et al. (2013)
1052	5605.19414	0.00180	0.30m - PEST[6]	TG Tan (TRESCA) re-analysed by Mancini et al. (2013)
1054	5606.77464	0.00022	EulerCam on Euler-Swiss	Lendl et al. (2013)
1055	5607.56241	0.00033	TRAPPIST	Lendl et al. (2013)
1074	5622.55057	0.00026	TRAPPIST	Lendl et al. (2013)
1076	5624.12787	0.00142	DFOSC on 1.54m Danish Telescope	Mancini et al. (2013)
1087	5632.80612	0.00025	EulerCam on Euler-Swiss	Lendl et al. (2013)
1116	5655.68222	0.00045	TRAPPIST	Lendl et al. (2013)
1135	5670.66976	0.00064	TRAPPIST	Lendl et al. (2013)
1144	5677.77038	0.00195	0.30m - PEST[6]	TG Tan (TRESCA) re-analyzed by Mancini et al. (2013)
1158	5688.81201	0.00333	0.30m - PEST[6]	TG Tan (TRESCA) re-analyzed by Mancini et al. (2013)
1159	5689.60276	0.00030	DFOSC on 1.54m Danish Telescope	Mancini et al. (2013)
1163	5692.75674	0.00255	0.30m - PEST[6]	TG Tan (TRESCA) re-analyzed by Mancini et al. (2013)
1164	5693.54639	0.00013	DFOSC on 1.54m Danish Telescope	Mancini et al. (2013)
1177	5703.79933	0.00411	0.30m - PEST[6]	TG Tan (TRESCA) re-analyzed by Mancini et al. (2013)
1178	5704.59078	0.00034	DFOSC on 1.54m Danish Telescope	Mancini et al. (2013)
1183	5708.53495	0.00015	DFOSC on 1.54m Danish Telescope	Mancini et al. (2013)
1228	5744.032190	0.000040	WFC3 on HST	Mandell et al. (2013)
1254	5764.54014	0.00125	CTIO 1m[8]	Cortés-Zuleta et al. (2020), analyzed by TLCM
1270	5777.16366	0.00022	IRAC on Spitzer	Wong et al. (2016)
1283	5787.41863	0.00023	IRAC on Spitzer	Wong et al. (2016)
1409	5886.81234	0.00208	0.30m - PEST[6]	TG Tan (TRESCA) re-analyzed by Mancini et al. (2013)
1421	5896.27611	0.00210	0.30m - PEST[6]	TG Tan (TRESCA) re-analyzed by Mancini et al. (2013)
1445	5915.20980	0.00065	0.30m - PEST[6]	TG Tan (TRESCA) re-analyzed by Mancini et al. (2013)
1450	5919.15485	0.00103	0.30m - PEST[6]	TG Tan (TRESCA) re-analyzed by Mancini et al. (2013)
1454	5922.30966	0.00555	0.30m - PEST[6]	TG Tan (TRESCA) re-analyzed by Mancini et al. (2013)
1552	5999.616301	0.0007	MMIRS on the Magellan II Telescope	Bean et al. (2013)
1580	6021.703740	0.000085	MMIRS on the Magellan II Telescope	Bean et al. (2013)
1595	6033.53645	0.00014	GROND[7]	Mancini et al. (2013)
1595	6033.53651	0.00007	GROND[7]	Mancini et al. (2013)
1595	6033.53643	0.00007	GROND[7]	Mancini et al. (2013)
1595	6033.53652	0.00009	GROND[7]	Mancini et al. (2013)
1590	6029.59251	0.00035	EulerCam on Euler-Swiss	Lendl et al. (2013)
1633	6063.51175	0.00030	TRAPPIST	Lendl et al. (2013)
1977	6334.87208	0.00053	0.25m - Rarotonga Observatory[3]	P. Evans (TRESCA)
1996	6349.86037	0.00081	0.25m - Rarotonga Observatory[3]	P. Evans (TRESCA)
2016	6365.63794	0.00010	DFOSC on 1.54m Danish Telescope	Cortés-Zuleta et al. (2020), analyzed by TLCM
2048	6390.87994	0.00043	0.25m - Rarotonga Observatory[3]	P. Evans (TRESCA)
2064	6403.50164	0.00022	DFOSC on 1.54m Danish Telescope	Cortés-Zuleta et al. (2020), analyzed by TLCM
2465	6719.82642	0.00050	0.25m - Rarotonga Observatory[3]	P. Evans (TRESCA)
2490	6739.551364	0.000046	IMACS on Magellan I Telescope	Espinoza et al. (2019)
2490	6739.54756	0.00029	0.30m - FRAM[9]	M. Mašek, K. Hoňková, J. Juryšek (TRESCA)

Notes. The time unit of each mid-transit time was checked and uniformized to BJD$_{TDB}$. Some digits are scientifically insignificant, but are left the same as in the reference papers.

[1] Beta Orionis Observatory, Argentina

[2] Cerro Armazones Observatory, Argentina

[3] Rarotonga Observatory, Cook Islands, New Zealand

[4] YSVP Observatory, South Australia, Australia

[5] Mount Albert Grammar School Observatory, New Zealand

[6] Perth Exoplanet Survey Telescope, West Australia, Australia

[7] Gamma Ray Burst Optical and Near-Infrared Detector on MPG/ESO, La Silla, Chile

[8] Cerro Tololo Inter-American Observatory, Chile

[9] F/Photometric Robotic Atmospheric Monitor telescope, Pierre Auger Observatory, Argentina, Ebr et al. (2014)

Table C.1. continued

Cycle number N	T_{mid} [days] BJD$_{TDB}$ - 2 450 000	Uncertainty [days]	Observations	Reference
2532	6772.67789	0.00052	TRAPPIST-South	Patra et al. (2020)
2537	6776.625805	0.000066	IMACS on Magellan I Telescope	Espinoza et al. (2019)
2792	6977.77653	0.00019	FORS2 on VLT	Sedaghati et al. (2015)
2930	7086.63573	0.00020	DFOSC on 1.54m Danish Telescope	Cortés-Zuleta et al. (2020), analyzed by TLCM
3044	7176.565524	0.000094	IMACS on Magellan I Telescope	Espinoza et al. (2019)
3351	7418.736819	0.000234	FORS2 on VLT	Sedaghati et al. (2017) re-analyzed by Petrucci et al. (2020)
3389	7448.712917	0.0000766	FORS2 on VLT	Sedaghati et al. (2017) re-analyzed by Petrucci et al. (2020)
3446	7493.67653	0.00024	DFOSC on 1.54m - Danish Telescope	Cortés-Zuleta et al. (2020), analyzed by TLCM
3477	7518.131796	0.000380	0.30m - PEST[†6]	Ivshina & Winn (2022) from Petrucci et al. (2020), TG Tan (TRESCA)
3513	7546.53025	0.00038	TRAPPIST-South	Patra et al. (2020)
3513	7546.52975	0.0002759	1.54m - EABA[†10]	Ivshina & Winn (2022) from Petrucci et al. (2020)
3518	7550.472701	0.0004477	1.54m - EABA[†10]	Ivshina & Winn (2022) from Petrucci et al. (2020)
3551	7576.504698	0.0007447	0.30m - FRAM[†9]	M. Mašek, K. Hoňková, J. Juryšek (TRESCA), re-analyzed by Ivshina & Winn (2022) from Petrucci et al. (2020)
3739	7724.807825	0.000828	2.15m - CASLEO[†11]	E. Fernández-Lajús, R. P. Di Sisto (TRESCA), re-analysed by Petrucci et al. (2020)
3758	7739.794151	0.000537	1.54m - EABA[†10]	Petrucci et al. (2020)
3806	7777.657426	0.001404	2.15m - CASLEO[†11]	Petrucci et al. (2020)
3815	7784.758917	0.000176	1.54m - EABA[†10]	Petrucci et al. (2020)
3825	7792.647526	0.000759	0.30m -FRAM[†9]	M. Mašek, K. Hoňková, J. Juryšek (TRESCA), re-analysed by Petrucci et al. (2020)
3830	7796.591396	0.000316	0.30m - FRAM[†9]	M. Mašek, K. Hoňková, J. Juryšek (TRESCA), re-analysed by Petrucci et al. (2020)
3830	7796.592241	0.000061	IMACS on Magellan I Telescope	Espinoza et al. (2019)
3834	7799.74616	0.00013	DFOSC on 1.54m - Danish Telescope	Cortés-Zuleta et al. (2020), analysed by TLCM
3896	7848.655592	0.000068	IMACS on Magellan I Telescope	Espinoza et al. (2019)
3901	7852.59809	0.00028	DFOSC on 1.54m - Danish Telescope	Cortés-Zuleta et al. (2020), analysed by TLCM
3906	7856.543843	0.000111	IMACS on Magellan I Telescope	Espinoza et al. (2019)
3906	7856.542283	0.000524	0.30m - FRAM[†9]	M. Mašek, K. Hoňková, J. Juryšek (TRESCA), re-analysed by Petrucci et al. (2020)
4127	8030.87615	0.00213	DFOSC on 1.54m - Danish Telescope	Cortés-Zuleta et al. (2020), analysed by TLCM
4189	8079.785673	0.0002142	1.54m - EABA[†10]	Petrucci et al. (2020)
4227	8109.763837	0.001527	2.15m - CASLEO[†11]	Petrucci et al. (2020)
4359	8213.887473	0.000243	0.30m - Ngileah Observatory[†12]	Petrucci et al. (2020) from C. Knight (TRESCA)
4757	8527.845759	0.000453	2.15m - CASLEO[†11]	Petrucci et al. (2020)
4778	8544.41145	0.0004479	TESS	Ivshina & Winn (2022)
4779	8545.19907	0.0003870	TESS	Ivshina & Winn (2022)
4780	8545.98902	0.0004050	TESS	Ivshina & Winn (2022)
4781	8546.77731	0.0004406	TESS	Ivshina & Winn (2022)
4782	8547.56698	0.0004338	TESS	Ivshina & Winn (2022)
4783	8548.35489	0.0004466	TESS	Ivshina & Winn (2022)
4784	8549.14427	0.0005019	TESS	Ivshina & Winn (2022)
4784	8549.144717	0.000534	0.32m - Bathurst Observatory[†13]	Petrucci et al. (2020) from A. Wünsche (TRESCA)
4785	8549.93223	0.0004417	TESS	Ivshina & Winn (2022)
4786	8550.72120	0.0004841	TESS	Ivshina & Winn (2022)
4787	8551.50999	0.0004451	TESS	Ivshina & Winn (2022)
4788	8552.29907	0.0004410	TESS	Ivshina & Winn (2022)
4789	8553.08782	0.0005204	TESS	Ivshina & Winn (2022)
4790	8553.87694	0.0004185	TESS	Ivshina & Winn (2022)
4791	8554.66562	0.0004163	TESS	Ivshina & Winn (2022)
4792	8555.45470	0.00011	TESS	Wong et al. (2020)
4795	8557.82154	0.0005118	TESS	Ivshina & Winn (2022)
4796	8558.60951	0.0005083	TESS	Ivshina & Winn (2022)
4797	8559.39917	0.0004697	TESS	Ivshina & Winn (2022)
4798	8560.18675	0.0004762	TESS	Ivshina & Winn (2022)
4799	8560.97736	0.0004474	TESS	Ivshina & Winn (2022)
4800	8561.76555	0.0004190	TESS	Ivshina & Winn (2022)
4801	8562.55365	0.0004069	TESS	Ivshina & Winn (2022)
4802	8563.34279	0.0004283	TESS	Ivshina & Winn (2022)
4803	8564.13199	0.0004019	TESS	Ivshina & Winn (2022)
4804	8564.92114	0.0005022	TESS	Ivshina & Winn (2022)
4805	8565.70943	0.0004585	TESS	Ivshina & Winn (2022)
4806	8566.49870	0.0003981	TESS	Ivshina & Winn (2022)
4807	8567.28776	0.0004885	TESS	Ivshina & Winn (2022)
4808	8568.07637	0.0004006	TESS	Ivshina & Winn (2022)
5714	9282.76417	0.0003798	TESS	Ivshina & Winn (2022)
5715	9283.55339	0.0004562	TESS	Ivshina & Winn (2022)
5716	9284.34253	0.0005261	TESS	Ivshina & Winn (2022)
5717	9285.13026	0.0004526	TESS	Ivshina & Winn (2022)
5718	9285.91981	0.0004843	TESS	Ivshina & Winn (2022)
5719	9286.70858	0.0004234	TESS	Ivshina & Winn (2022)
5720	9287.49712	0.0004700	TESS	Ivshina & Winn (2022)
5721	9288.28588	0.0004688	TESS	Ivshina & Winn (2022)
5722	9289.07500	0.0004201	TESS	Ivshina & Winn (2022)
5723	9289.86356	0.0003895	TESS	Ivshina & Winn (2022)
5724	9290.65264	0.0004974	TESS	Ivshina & Winn (2022)
5725	9291.44097	0.0004855	TESS	Ivshina & Winn (2022)
5726	9292.23008	0.0004141	TESS	Ivshina & Winn (2022)

[†9] F/Photometric Robotic Atmospheric Monitor telescope, Pierre Auger Observatory, Argentina
[†10] Estación Astrofísica de Bosque Alegre, Argentina
[†11] Complejo Astronómico El Leoncito, Argentina
[†12] Ngileah Observatory, New Zealand
[†13] Bathurst Observatory, New South Wales, Australia

Table C.1. continued.

Cycle number N	T_{mid} [days] BJD$_{TDB}$ - 2.450.000	Uncertainty [days]	Observations	Reference
4824	8580.69724	0.00040	TRAPPIST-South	Patra et al. (2020)
4829	8584.641667	0.000268	1.54m - EABA[†9]	Petrucci et al. (2020)
5730	9295.38506316	0.0005686	TESS	Rosário et al. (2022)
5731	9296.17539	0.0004310	TESS	Ivshina & Winn (2022)
5732	9296.96307	0.0004743	TESS	Ivshina & Winn (2022)
5733	9297.75141	0.0005115	TESS	Ivshina & Winn (2022)
5734	9298.54007	0.0004491	TESS	Ivshina & Winn (2022)
5735	9299.32928	0.0004109	TESS	Ivshina & Winn (2022)
5736	9300.11829	0.0004992	TESS	Ivshina & Winn (2022)
5737	9300.90761	0.0004934	TESS	Ivshina & Winn (2022)
5738	9301.69654	0.0004158	TESS	Ivshina & Winn (2022)
5739	9302.48453	0.0004775	TESS	Ivshina & Winn (2022)
5740	9303.27451	0.0004810	TESS	Ivshina & Winn (2022)
5741	9304.06354	0.0004313	TESS	Ivshina & Winn (2022)
5742	9304.85186	0.0004499	TESS	Ivshina & Winn (2022)
6258	9711.89359	0.00034	0.30m - Ngileah Observatory[†12]	C. Knight (TRESCA), analysed by TLCM
6272	9722.93627	0.00084	0.30m - Ngileah Observatory[†12]	C. Knight (TRESCA), analysed by TLCM
6505	9906.734941	0.00058	0.43m - Deep Sky, Chile	Y. Jongen (TRESCA)
6141	9619.60147	0.00039	0.43m - Deep Sky, Chile	J.-P. Vignes (TRESCA)
6145	9622.756750	0.00042	0.43m - Deep Sky, Chile	J.-P. Vignes (TRESCA)
6557	9947.75209	0.00114	0.15m - Observatorio Vuelta por el Universo[†14]	M. Anzola (TRESCA)

[†10] Estación Astrofísica de Bosque Alegre, Argentina
[†12] Ngileah Observatory, New Zealand
[†14] Observatorio Vuelta por el Universo, Argentina

Table C.2. Occultations found in the literature.

Cycle number N	T_{mid} [days] BJD$_{TDB}$ - 2 450 000	Uncertainty [days]	Observations	Reference
2	4777.313572	$+0.00013$ -0.00014	HAWK-I (VLT)	Anderson et al. (2010)
185	4921.66849	0.00190	HAWK-I (VLT)	Gibson et al. (2010)
1018	5578.7684	0.0039	ULTRACAM on NTT	Burton et al. (2012)
1199	5721.5508	$+0.0028$ -0.0031	DFOSC on 1.54m - Danish Telescope	Mancini et al. (2013)
1269	5776.77020	0.00083	IRAC on Spitzer	Wong et al. (2016)
1270	5777.55733	0.00092	IRAC on Spitzer	Wong et al. (2016)
1282	5787.02383	0.00077	IRAC on Spitzer	Wong et al. (2016)
1283	5787.81228	0.00076	IRAC on Spitzer	Wong et al. (2016)
1549	5997.6440	0.001	MMIRS on Magellan II telescope	Bean et al. (2013)
1582	6023.6763	0.001	MMIRS on Magellan II telescope	Bean et al. (2013)

Notes. The cycle number is referred to the previous transit (half phase before the occultation). Light travel time across the system (around 16.3 s) is subtracted from all mid-occultation times.

Appendix D: Tables of RVs

Table D.1. Radial velocity of WASP-19Ab system.

Instr. ID	BJD$_{TDB}$ $-2\,450\,000.0$	RV_{obs} [km s^{-1}]	Uncertainty [km s^{-1}]
1	4616.46326	20.965	0.0218
1	4623.46713	20.712	0.0289
1	4624.46191	21.019	0.0220
1	4652.46587	20.512	0.0210
1	4653.46543	20.770	0.0231
1	4654.46530	21.007	0.0219
1	4656.47564	20.511	0.0193
1	4657.46805	20.902	0.0386
1	4658.46376	21.008	0.0302
1	4660.46652	20.604	0.0400
1	4661.46434	20.974	0.0217
1	4662.46549	20.922	0.0191
1	4663.46607	20.547	0.0188
1	4664.46573	20.645	0.0362
1	4665.46709	21.077	0.0305
1	4827.74752	20.683	0.0188
1	4832.74362	21.050	0.0242
1	4833.66844	20.860	0.0212
1	4834.67693	20.548	0.0191
1	4837.67024	20.726	0.0227
1	4838.68496	20.562	0.0244
1	4839.70064	20.936	0.0185
1	4890.61491	20.637	0.0187
1	4894.68743	20.518	0.0290
1	4895.69238	20.894	0.0179
1	4896.66180	21.041	0.0145
1	4897.65715	20.674	0.0175
1	4898.66015	20.544	0.0197
1	4939.53373	20.578	0.0164
1	4940.52747	20.642	0.0154
1	4941.53928	20.996	0.0156
1	4942.52421	20.899	0.0169
1	4943.53594	20.559	0.0191
1	4944.52955	20.798	0.0155
2	4972.4990	20.8874	0.0176
2	4973.4656	20.6042	0.0182
2	4999.4865	20.5571	0.0341
3	5242.6892	20.7469	0.0036
3	5242.8465	21.0203	0.0050
3	5243.6598	21.0391	0.0042
3	5243.8250	20.9547	0.0043
3	5244.7229	20.7355	0.0031
3	5247.7159	21.0254	0.0088
3	5272.5453	20.5741	0.0044
3	5272.7784	20.9778	0.0052
3	5274.5336	21.0391	0.0073
3	5274.6155	20.9318	0.0124
3	5274.6232	20.9129	0.0112
3	5274.6307	20.8819	0.0094
3	5274.6383	20.8842	0.0088
3	5274.6459	20.8711	0.0084
3	5274.6533	20.8914	0.0086
3	5274.6610	20.8473	0.0094
3	5274.6687	20.8214	0.0100
3	5274.6762	20.7819	0.0108
3	5274.6838	20.7568	0.0118
3	5274.6915	20.7315	0.0108
3	5274.6991	20.7138	0.0103

Notes. The indices of the observations are the same as in Fig. 1 and Sect. 4.

Table D.1. continued.

Instr. ID	BJD$_{TDB}$ $-2\,450\,000.0$	RV_{obs} [km s^{-1}]	Uncertainty [km s^{-1}]
3	5274.7066	20.7262	0.0106
3	5274.7142	20.7093	0.0104
3	5274.7218	20.7151	0.0118
3	5274.7296	20.7056	0.0120
3	5274.7371	20.6582	0.0116
3	5274.7446	20.6687	0.0104
3	5274.7522	20.6387	0.0119
3	5274.7599	20.6452	0.0113
3	5274.7675	20.6136	0.0105
3	5274.7748	20.6079	0.0106
3	5274.7826	20.5771	0.0123
3	5274.8224	20.5707	0.0069
3	5275.5229	20.6841	0.0052
3	5275.7903	20.6841	0.0077
3	5276.5154	20.5850	0.0062
4	5338.47873	0.13439	0.01522
4	5338.48498	0.11220	0.01214
4	5338.49280	0.09687	0.01226
4	5338.50068	0.06777	0.01130
4	5338.50859	0.05913	0.01108
4	5338.51623	0.04541	0.01068
4	5338.52418	0.00975	0.01071
4	5338.53215	0.00564	0.01140
4	5338.53993	0.00808	0.01054
4	5338.54787	0.06322	0.01216
4	5338.55585	-0.00877	0.01121
4	5338.56351	-0.01221	0.01281
4	5338.57167	-0.05589	0.01214
5	6018.8117983	-0.168663	0.003077
5	6290.1405875	-0.137606	0.003032
5	6318.9215917	0.306274	0.002318
6	8498.59068874	20.82646	0.00818
6	8498.60180095	20.7993	0.00716
6	8498.61279395	20.7785	0.00819
6	8498.62459247	20.76231	0.00651
6	8498.63454273	20.76321	0.0145
6	8498.63972473	20.77791	0.01274
6	8498.64464221	20.79349	0.01338
6	8498.64956116	20.73967	0.01424
6	8498.65436899	20.69906	0.01462
6	8498.65942065	20.69273	0.01402
6	8498.66430660	20.67341	0.01475
6	8498.66926300	20.63671	0.01324
6	8498.67428582	20.61285	0.01011
6	8498.67907061	20.60608	0.00899
6	8498.68407176	20.61570	0.00897
6	8498.68899962	20.61782	0.00781
6	8498.69387378	20.62464	0.00745
6	8498.70087685	20.61316	0.00457
6	8498.71044096	20.60040	0.00456
6	8498.71956719	20.59894	0.00435
6	8498.72920549	20.56458	0.00439
6	8498.73862103	20.55429	0.00399
6	8546.70109917	20.81404	0.00542
6	8546.71810796	20.77644	0.00864
6	8546.73102276	20.74880	0.00911
6	8546.74715133	20.74357	0.00749
6	8546.75677225	20.74175	0.01771
6	8546.76244128	20.70465	0.00183
6	8546.76773966	20.74182	0.02089
6	8546.77334046	20.66661	0.01599
6	8546.77859110	20.65585	0.01502

Table D.1. continued.

Instr. ID	BJD$_{TDB}$ $-2\,450\,000.0$	RV_{obs} [km s^{-1}]	Uncertainty [km s^{-1}]
6	8546.78395751	20.66390	0.01514
6	8546.78909247	20.57827	0.02002
6	8546.79475258	20.59739	0.01890
6	8546.80036398	20.55623	0.02008
6	8546.80553459	20.63033	0.01792
6	8546.81107313	20.62332	0.01776
6	8546.81638670	20.59751	0.01665
6	8546.82327218	20.61843	0.01500
6	8546.83186421	20.50721	0.01337
6	8546.84018927	20.57332	0.01128
6	8546.84855560	20.55209	0.01556
6	8546.85730223	20.51568	0.01358
6	8565.63006930	20.85050	0.00419
6	8565.64050392	20.83263	0.00415
6	8565.65068188	20.81295	0.00392
6	8565.66089612	20.79194	0.00431
6	8565.67121537	20.76472	0.00420
6	8565.68117929	20.77662	0.00364
6	8565.68892203	20.78292	0.00850
6	8565.69398195	20.76429	0.00868
6	8565.69899674	20.74261	0.00836
6	8565.70399522	20.72989	0.00813
6	8565.70895259	20.68067	0.00844
6	8565.71404306	20.66203	0.00896
6	8565.71903842	20.64335	0.00830
6	8565.72397488	20.61127	0.00858
6	8565.72902717	20.61737	0.00865
6	8565.73403920	20.61288	0.00769
6	8565.73901729	20.62037	0.00740
6	8565.74406099	20.61360	0.00733
6	8565.75100246	20.60935	0.00391
6	8565.75992839	20.59612	0.00389
6	8565.76886384	20.57339	0.00399
6	8565.77776409	20.56269	0.00403
6	8565.78359563	20.54291	0.01537
7	8860.65868965	20.80633	0.00247
7	8860.66953784	20.78622	0.00219
7	8860.68086427	20.77083	0.00224
7	8860.69232959	20.75252	0.00205
7	8860.70329540	20.73853	0.00201
7	8860.71235224	20.76021	0.00306
7	8860.71764990	20.75988	0.00329
7	8860.72296232	20.74915	0.00298
7	8860.72842374	20.72062	0.00296
7	8860.73374936	20.68917	0.00305
7	8860.73902683	20.65960	0.00289
7	8860.74434671	20.62669	0.00289
7	8860.74960873	20.60702	0.00300
7	8860.75500031	20.59131	0.00293
7	8860.76033814	20.59485	0.00285
7	8860.76571960	20.60629	0.00280
7	8860.77096557	20.60589	0.00288
7	8860.77847463	20.59486	0.00195
7	8860.78808536	20.57681	0.00200
7	8860.79770303	20.56175	0.00208
7	8860.80730381	20.54011	0.00213
7	8860.81678339	20.52403	0.00211
8	8885.81831	21.05010	0.00590
8	8886.63492	21.04724	0.00588
8	8886.74637	20.91119	0.00495

Table D.1. continued.

Instr. ID	BJD$_{TDB}$ $-2\,450\,000.0$	RV_{obs} [km s^{-1}]	Uncertainty [km s^{-1}]
8	8887.70434	20.62644	0.01004
8	8887.78381	20.61007	0.00596
8	8888.61415	20.65507	0.00593
8	8888.65498	20.69769	0.00576
8	8889.67038	21.11750	0.00694
8	8889.82412	21.04723	0.00663
8	8893.66960	21.10599	0.01208
8	8893.76426	21.04400	0.00549
8	8893.83745	20.91112	0.00615
8	8894.63550	20.90340	0.00821
8	8894.69107	20.75424	0.00781
8	8894.77058	20.62550	0.00732
8	8897.68716	21.06761	0.00712
8	8897.75751	20.97271	0.00668
8	8899.85008	21.01457	0.00592